GEOLOGICAL JOURNAL
Geol. J. **49**: 599–616 (2014)
Published online 26 May 2014 in Wiley Online Library
(wileyonlinelibrary.com). DOI: 10.1002/gj.2570

Ore genesis of the unusual Talate Pb–Zn(–Fe) skarn-type deposit, Altay, NW China: constraints from geology, geochemistry and geochronology

DENG-FENG LI[1,2], LI ZHANG[1]*, HUA-YONG CHEN[1], YI ZHENG[1,3], PETE HOLLINGS[4], CHENG-MING WANG[1,2] and JING FANG[1,2]

[1] *Key Laboratory of Mineralogy and Metallogeny, Chinese Academy of Sciences, Guangzhou, China*
[2] *Graduate University of Chinese Academy of Sciences, Beijing, China*
[3] *Department of Earth Sciences, Sun Yat-sen University, Guangzhou, China*
[4] *Department of Geology, Lakehead University, Thunder Bay, Ontario, Canada*

The Talate ore field is located in the Abagong polymetallic metallogenic belt of the Altay Orogen, NW China. Lenticular ore bodies occur in the Kangbutiebao Formation, a package of intermediate-felsic marine volcanic rocks and terrigenous clastic sedimentary-carbonate rocks. Skarn alteration (mainly garnet) is present in both ore and wall rocks, especially the carbonate rocks. The mineral assemblages and cross-cutting relationships of veins allow the alteration and mineralization process to be divided into four stages. From early to late, these are the early skarn (E-skarn), the late skarn with quartz–magnetite veins (QM), the quartz–sulphide (QS) and the quartz–carbonate (QC) assemblages. Quartz crystals are important gangue minerals in the latter three stages, in which four distinct compositions of fluid inclusions are identified based on petrography, microthermometry and laser Raman microspectroscopy, namely aqueous inclusions (W-type), pure CO_2 inclusions (PC-type), CO_2-rich inclusions (C-type) and daughter mineral-bearing inclusions (S-type). Microthermometric data and laser Raman analyses show that the quartz crystals from the QM stage contain all four inclusion types, with the W-type being predominant. Homogenization temperatures range between 271 and 426 °C. The salinities of the W- and C-type fluid inclusions range from 0.5 to 22.4 wt.% NaCl eqv., whereas the S-type fluid inclusions in the QM stage range from 31 to 41 wt.% NaCl eqv. Daughter minerals in the fluid inclusions include halite, sylvite, pyrite and calcite. Quartz from the QS stage (main mineralization stage) contains the W-, C- and PC-type inclusions, which are homogenized at temperatures of 204–269 °C, with salinities of 0.2–15.6 wt.% NaCl eqv. Only W-type fluid inclusions have been identified in the QC stage. These yielded homogenizing temperatures of 175–211 °C and salinities of 1.1–9.9 wt.% NaCl eqv. The C-type fluid inclusions of the main (QS) mineralization stage yield trapping pressures of 107–171 MPa, corresponding to a depth of 4–6 km. The sulphur isotope values (−1.7‰ and −6.6‰) imply that the QS stage may not be directly associated with the early skarn (−7.4‰) and quartz–magnetite stages (−4.8‰ and −5.0‰), though the QS stage is probably dominated by magmatic-hydrothermal fluids. $^{40}Ar/^{39}Ar$ isotope plateau ages of 227.6 and 214.1 Ma for biotite separated from the QM and QS stages are significantly younger than the host Kangbutiebao Formation (*ca*. 410 Ma). The Talate Pb–Zn(–Fe) deposit is interpreted to be an unusual skarn-type system formed in a continental collision orogeny. Copyright © 2014 John Wiley & Sons, Ltd.

Received 20 November 2013; accepted 15 April 2014

KEY WORDS Pb–Zn(–Fe) deposit; fluid inclusion geochemistry; sulphur isotope; $^{40}Ar/^{39}Ar$ geochronology; Chinese Altay

1. INTRODUCTION

Skarn-type (or contact metasomatic) deposits occur throughout the world and have been mined for a variety of elements (Fe, W, Cu, Pb, Zn, Mo, Ag, Au, U, REE, F, B and Sn). Over the past two decades, large numbers of skarn-type deposits have been discovered all over the world (Sato, 1980; Shelton, 1983; Meinert *et al*., 1997; Lu *et al*., 2003; Baker *et al*., 2004; Chen *et al*., 2007; Shi *et al*., 2009; Yang *et al*., 2013a). Although the majority of the deposits are found in lithologies containing at least some limestone, they can form in most rock types, including shale (Einaudi and Burt, 1982; Meinert, 1983; Jamtveit and Andersen, 1993), sandstone (Takeuchi, 1994; Forster *et al*., 2004; Ganino *et al*., 2008), granite (Watters, 1958; El-Sharkawi and Dearman, 1966; Romer and Soler, 1995), basalt (Kunzmann, 1999) and komatiite (Meinert, 1992).

Distinguishing between reworked deposits with skarn alteration and primary skarn deposits in metamorphic terranes is sometimes difficult but is essential for establishing genetic models. Reworked deposits may form prior to regional metamorphism or magmatism, and many

*Correspondence to: L. Zhang, Guangzhou Institute of Geochemistry, Chinese Academy of Sciences, P.O. Box 1131, Tianhe District, Guangzhou 510640, Guangdong, China. E-mail: zhangli@gig.ac.cn

are of syngenetic origin [such as reworked volcanogenic massive sulphide (VMS) deposit, Wan *et al*., 2010]. In contrast, skarn deposits normally are epigenetic hydrothermal deposits that formed as a result of a contact-metasomatism (Pan and Dong, 1999; O'Neill *et al*., 2002; Chen *et al*., 2007; Pirajno, 2009; Wan *et al*., 2010). Distinguishing between the two is essential, because it provides insights into the geological processes involved in mineralization and provides a basis for developing exploration models.

Large numbers of Pb–Zn and Fe deposits occur in the southern Chinese Altay Mountains, including Keketale (reworked VMS Pb–Zn with skarn alteration), Mengku (skarn Fe deposit) and Sawusi (skarn Pb–Zn deposit) (Wang *et al*., 1998; Goldfarb *et al*., 2003; Li *et al*., 2003; Jiao *et al*., 2006; Xu *et al*., 2007; Wan *et al*., 2010; Liu *et al*., 2011, 2012). These deposits are hosted within the volcanic clastic rocks, tuffs and carbonates of the Kangbutiebao Formation (Wang *et al*., 2000; Cheng *et al*., 2009). However, multiple regional metamorphic and magmatic events have reworked these deposits (Wang *et al*., 2000), resulting in controversy over their genesis. In addition, the age of many deposits hosted in the Kangbutiebao Formation is poorly constrained, and their relationship with the host rocks remains uncertain.

The Talate Pb–Zn(–Fe) deposit, located in the Kelan Basin on the southern edge of Chinese Altay in Xinjiang Province, NW China, is currently being explored, and the Pb and Zn resources have reached medium scale (~0.2 million tons Pb and Zn, Yuan *et al*., 2011). The Talate ore bodies occur within the volcanic rocks and carbonates of the Kangbutiebao Formation and have been classified as a VMS deposit similar to the other Pb–Zn deposits in the Abagong metallogenic belt (Ye and Fu, 1998). However, the details of the ore-forming fluids, the petrogenesis and geochronology have not been previously documented. This paper presents fluid inclusion data, $^{40}Ar/^{39}Ar$ ages and sulphur isotope data to further clarify ore genesis of the Talate Pb–Zn(–Fe) deposit and uses those data, together with those of other researchers, to propose a new metallogenic model for the Kelan Basin and provide a guide for future exploration in the southern Chinese Altay.

2. REGIONAL GEOLOGY

The Central Asian Orogenic Belt (CAOB: Kroener *et al*., 2013), known as the Altay, is a late Palaeozoic (320–250 Ma) or Hercynian (Variscan) subduction-related accretionary orogen (Chen *et al*., 2012) formed by accretion of island arcs, ophiolites, oceanic islands, seamounts, accretionary wedges, oceanic plateaus and microcontinents (Windley *et al*., 2007; Cai *et al*., 2011). The southern margin of the Altay Mountains contains several volcanic sedimentary basins. The Kelan Basin is a volcanic sedimentary basin (Fig. 1A and B) located in the Late Palaeozoic Altay active continental margin and hosts a number of significant deposits in the Abagong metallogenic belt (Ye and Fu, 1998; Chen *et al*., 2001; Wan *et al*., 2011). Rocks exposed in the Kelan Basin include the upper Silurian Kulumuti Group, the lower Devonian Kangbutiebao Formation and the middle Devonian Altay Formation. The Kulumuti Group consists of schist, gneiss and migmatites, which are unconformably overlain by the Kangbutiebao Formation, which is composed of sedimentary and intermediate-felsic volcanic rocks deposited in an extensional environment along an active continental margin. The Altay Formation comprises a series of metamorphosed sandstone, schist and phyllite. All the Devonian rocks were folded and metamorphosed to greenschist facies during the Hercynian Orogeny with a typical metamorphic mineral assemblage of biotite + chlorite + epidote + actinolite. The intrusive rocks within the basin were emplaced in the Ordovician, Permian and Triassic, with a small number in the Jurassic (Fig. 1).

The principal structure in the Kelan Basin is the Altay duplex syncline, which strikes northwest for ~50 km and dips to the northeast at 50–70°. The southwest limb displays a normal succession whereas the northeast limb is overturned. The core of the syncline is made up of the middle Devonian Altay Formation, which is younger than the limbs composed of the Kangbutiebao Formation and Kulumuti Group. The northwest-trending faults in the Kelan Basin typically form boundaries between the different stratigraphic units. For example, the Keyingong Fault separates the Kulumuti Group and the Kangbutiebao Formation whereas the Abagong Fault separates the Kangbutiebao and Altay formations (Fig. 1C). These faults also appear to control the spatial distribution of ore deposits, e.g. the Dadonggou Pb–Zn deposit, Wulasigou Pb–Zn and Cu deposit, Qiaxia Fe–Cu deposit, Sarekuobu Au deposit, Tiemurte Pb–Zn deposit, Tuomoerte Fe (Mn) deposit, Abagong Fe deposit and the Talate Pb–Zn(–Fe) deposit (Fig. 1C), which all occur along the Abagong and Keyingong fault belts. The lower Devonian Kangbutiebao Formation is the main host rock for the mineralization and has yielded SHRIMP zircon U–Pb ages of 413–407 Ma (Chai *et al*., 2009).

3. DEPOSIT GEOLOGY

The Talate Pb–Zn(–Fe) deposit is located in the southeastern part of the Abagong Pb–Zn–Fe district (Fig. 1D) and is characterized by higher Zn grades than other Pb–Zn–Fe occurrences in the area. It currently contains a reserve of 0.2 million tons of ore with an average grade of 7.93% total Pb and Zn (at a 0.35% cut-off; Yuan *et al*., 2011). The Talate Pb–Zn(–Fe) deposit is hosted in the lower section of the lower Devonian Kangbutiebao Formation. In the vicinity

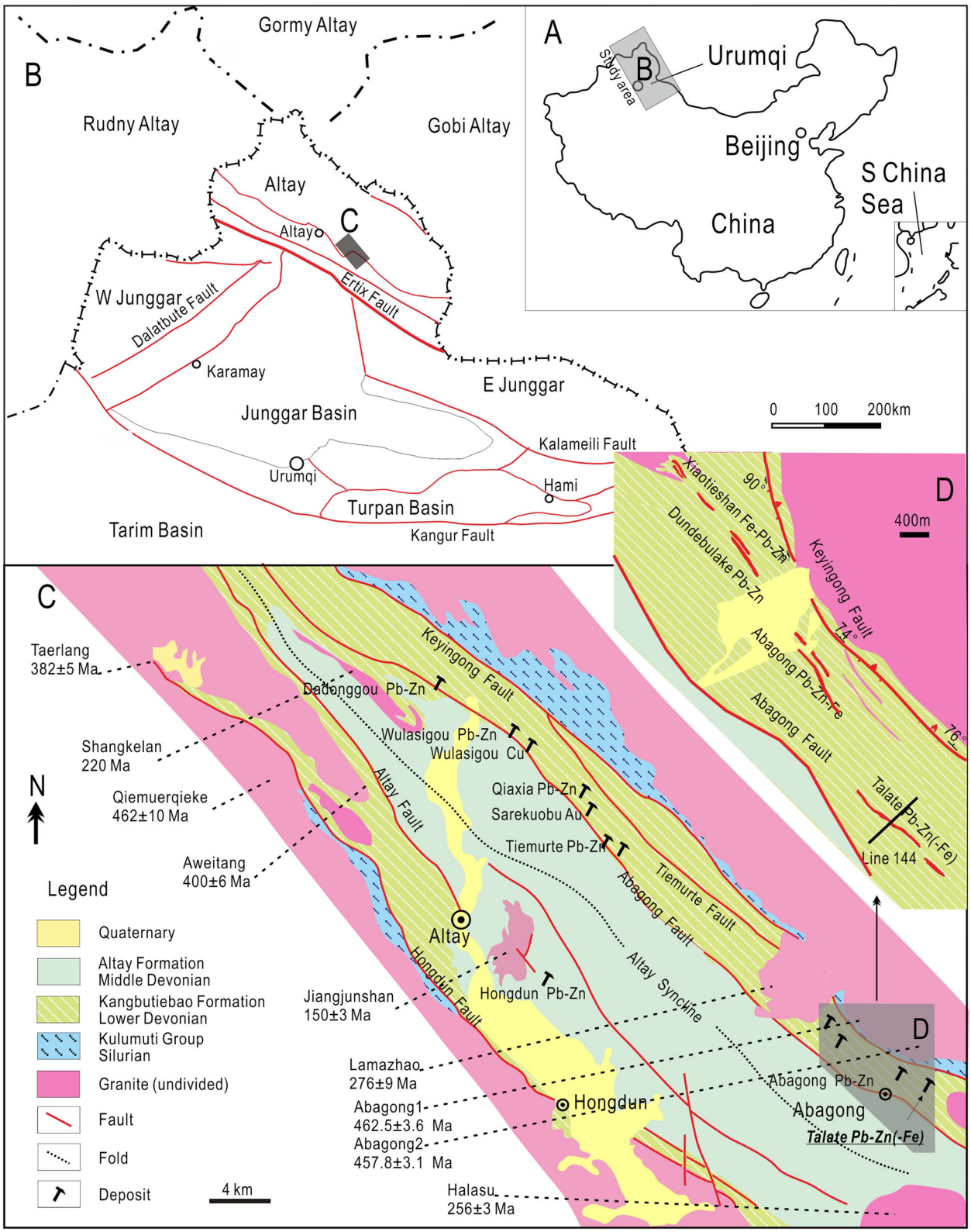

Figure 1. Sketch map of the Abagong metallogenic belt in Kelan Basin in Xinjiang Province, NW China (modified after Geological Team 706 of the Xinjiang Bureau of Nonferrous Metals, 2000). Important plutons are marked with their names and ages (Chen and Jahn, 2002; T. Wang *et al*., 2005, 2006, 2007, 2009; Cai *et al*., 2007; Liu *et al*., 2008), **A** and **B** show the location of Kelan Basin in Xinjiang Province, NW China; **C**, sketch map of the Abagong metallogenic belt; **D**, sketch map of the Talate Pb–Zn(–Fe) deposit. This figure is available in colour online at wileyonlinelibrary.com/journal/gj

of the deposit, the Kangbutiebao Formation comprises rhyolitic–dacitic tuff, marble, sandstone and volcanic breccia tuff. Due to movement along the Abagong and Keyingong faults, rocks in the Abagong polymetallic metallogenic belt are generally brecciated and silicified. Felsic intrusions emplaced in the vicinity of the deposit are dominated by the Lamazhao I- to A-type granites (276 ± 9 Ma; Wang *et al*., 2005), the Abagong granitic gneiss (462.5 ± 3.6 Ma; Liu *et al*., 2008) and the Halasu plagiogranites (256 ± 3 Ma; T. Wang *et al*., 2009).

The largest orebody, with a length of 920 m and width of 11 m, is lenticular in shape and hosted in felsic volcanic lava and metaconglomerate (Fig. 2). Dominant ore minerals at Talate include sphalerite, pyrite, pyrrhotite, galena and magnetite with minor chalcopyrite and arsenopyrite. The gangue minerals are mainly garnet, quartz, tremolite, actinolite, diopside, tourmaline, epidote, calcite and biotite (Fig. 3). Ore textures vary from massive to banded and disseminated.

The wallrock alteration is mainly skarnization, pyritization, carbonatization and silicification. The Pb–Zn mineralization is spatially related to skarns, and the dominant skarn mineral assemblages are garnet, tremolite, actinolite and epidote. The sulphide minerals are mainly disseminated within the host rock, with rare banded and veinlet structures. The paragenetic sequences of the Talate Pb–Zn deposit are shown in Figure 4.

Based on the mineral assemblages and cross-cutting relationships, the alteration and mineralization process at Talate can be divided into four stages; these are the early skarn stage (E-skarn) (Fig. 3A–C), late skarn with quartz–magnetite (QM) stage (Fig. 3D–F), quartz–sulphide (QS) stage (Fig. 3G–J) and quartz–carbonate (QC) stage (Fig. 3K and L).

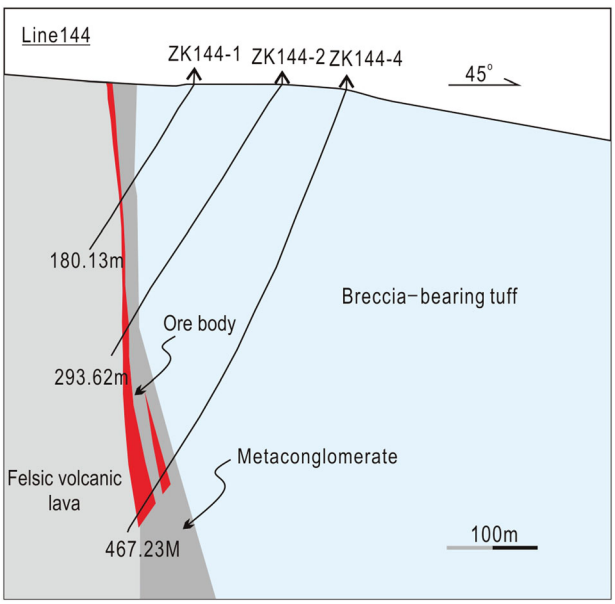

Figure 2. Sketch geological profile for exploration line 144 of the Talate Pb–Zn(–Fe) deposit. This figure is available in colour online at wileyonlinelibrary.com/journal/gj

Anhydrous minerals such as garnet and diopside characterize the E-skarn stage. Garnet is characterized by coarser grain textures, and many of them have undergone later hydrothermal replacement (Fig. 3J). The QM stage is magnetic and dominated by hydrous silicate minerals such as hornblende, tremolite, actinolite and epidote (Fig. 3D and E). Quartz–magnetite veins with small amounts of pyrite are very common in this stage and typically display a crack-sealing texture as described by Sibson *et al*. (1988) (Fig. 3F). The magnetite typically fills those cracks in garnet or occurs between garnet crystals, indicating that magnetite is paragenetically younger than garnet (Fig. 3H and J).

The quartz–sulphide stage (i.e. the main Pb–Zn mineralization) cross-cuts the skarn alteration and is characterized by sphalerite, pyrite, pyrrhotite and galena, with minor chalcopyrite, malachite, pentlandite and arsenopyrite. In Figure 3J, pyrite and chalcopyrite veinlets cut across the garnet. The biotite coexisting with pyrite and quartz in the QS stage is an ideal mineral for Ar–Ar geochronology (Fig. 3I). The quartz–carbonate stage is dominated by quartz–calcite veins and cross-cuts both the E-skarn and QM stages (Fig. 3K). This stage is characterized by subhedral pyrite that coexists with calcite (Fig. 3L).

4. FLUID INCLUSIONS

4.1. Methodology

Samples representing different mineralization stages were collected from the southern section of the ore body, and all the samples were polished on both sides. Two hundred and ninety-six fluid inclusions (FI) from seven samples from the QM stage, the QS stage and the QC stage were selected for fluid inclusion petrography and microthermometry, but no FIs were found in the E-skarn stage.

Fluid inclusion microthermometry was undertaken at the Institute of Geology and Geophysics, Chinese Academy of Sciences (IGGCAS), Beijing, using a Linkam THMSG600 and THMSG1500 freezing and heating system, matched with a German Zeiss microscope. A US fluid INC standard was used to correct the temperatures at −56.6, 0.0 and 374.1 °C. Fluid inclusions were initially cooled to −100 °C at the rate of −5 °C/min and held for 1 min to make sure the FI was frozen. Inclusions were then warmed at 5 °C/min to −60 °C where they were held for 1 min; the warming rate was reduced to 0.5 °C/min, and when the temperature reached −56.6 °C, it was held for another minute. The temperature was increased at 1 °C/min until 10 °C was reached. Finally, the sample was warmed at a rate of 5 °C/min to 150 °C and then at 3 °C/min until close to the homogeneous phase

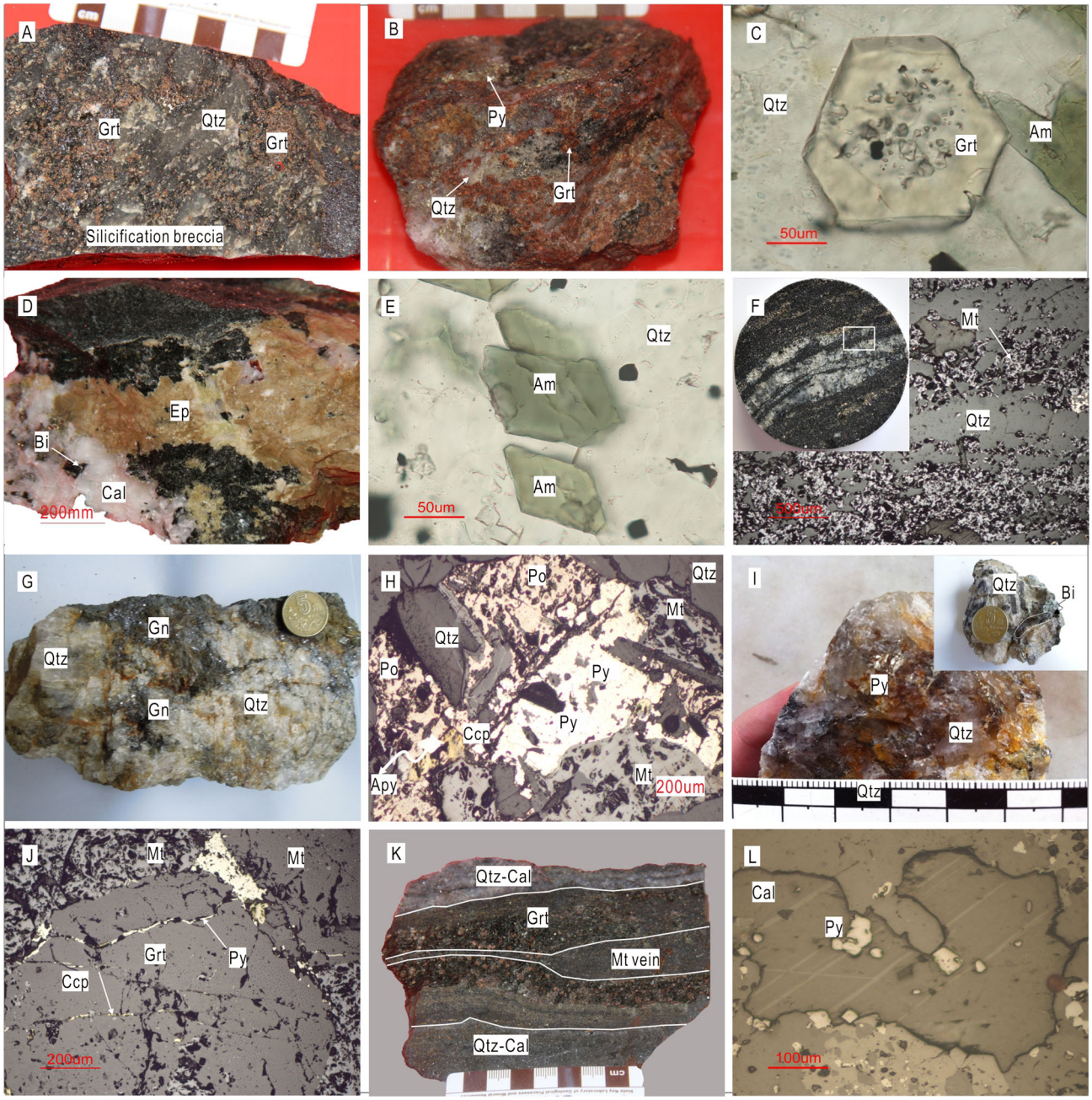

Figure 3. Photographs showing ore samples, mineral assemblages and paragenetic relationships of the Talate Pb–Zn(–Fe) deposit, **A**, garnet skarn with silicification breccia; **B**, euhedral garnet is partly replaced by quartz; **C**, euhedral garnet and amphibole under plane-polarized light; **D**, QM stage quartz veinlets brecciated by epidote, quartz and calcite; **E**, euhedral amphibole under plane-polarized light; **F**, banded magnetite–quartz veins; **G**, quartz–pyrite veins in the QS stage; **H**, magnetite in QM stage is replaced by polymetallic sulphide in the QS stage; **I**, biotite, quartz and pyrite in the QS stage; **J**, pyrite and chalcopyrite stringers filling between/in gangue minerals such as garnet; **K**, quartz–calcite veins in the QC stage; **L**, calcite and pyrite in the QC stage; abbreviations: Am—amphibole, Apy—arsenopyrite, Bi—biotite, Cal—calcite, Ccp—chalcopyrite, Ep—epidote, Gn—galena, Grt—garnet, Qtz—quartz, Mt—magnetite, Po—pyrrhotite, Py—pyrite, Sp—sphalerite. This figure is available in colour online at wileyonlinelibrary.com/journal/gj

transition point at which time a lower rate of about 0.5–1 °C/min was used.

Salinities of aqueous inclusions were calculated using the equation of Bodnar (1993) for the NaCl–H_2O system. Salinities of halite daughter mineral-bearing inclusions were identified using the reference data and methodology of Vityk *et al.* (1994). Salinities of CO_2-rich inclusions were calculated using the equations of Collins (1979) for the CO_2–NaCl–H_2O system.

Vapour and liquid compositions were measured at the Raman Spectroscopy Laboratory of the Institute of Geology

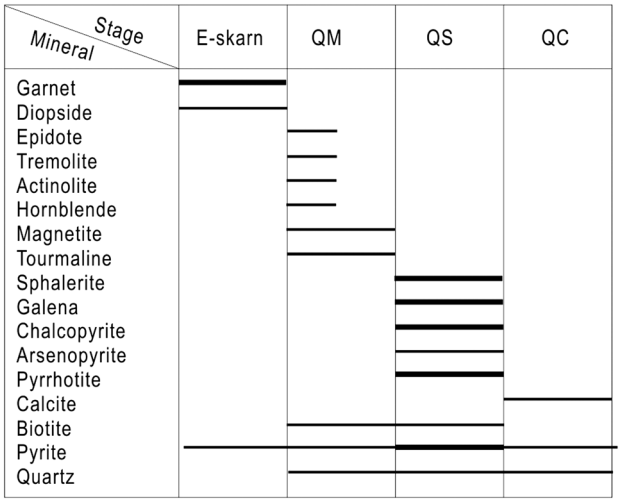

Figure 4. Paragenetic sequence of the Talate Pb–Zn(–Fe) deposit.

and Geophysics, Chinese Academy of Sciences (IGGCAS), Beijing. An excitation wavelength of 532 nm was used with the Ar^+ ion laser operating at 44 mW. The spectra were measured with 3 s counting times and counted every 1 cm^{-1} from 500 to 4000 cm^{-1}. The laser beam had a spot size of approximately 1 µm with spectral resolution of 0.65 cm^{-1}. It was calibrated on pure silicon produced in France with standard Raman shift of 520.7 cm^{-1}. For peak standards such as CO_2, CH_4 and N_2, see Frezzotti *et al.* (2012).

To identify the daughter minerals in fluid inclusions, SEM/EDS (scanning electron microscopy/energy dispersive spectrometer) was conducted in the Instrumental Analysis and Research Centre Electron Microscope Lab, Sun Yat-sen University (Guangzhou), using a Quanta 400 Thermal FE Environment Scanning Electron Microscope with an analysable element range of ^{4}Be–^{92}U. The EDS analyses are semi-qualitative.

4.2. *Classification and distribution of fluid inclusions*

The QM stage quartz veins show lumps or lenticular shape (Fig. 3D) due to deformation and are characterized by undulatory extinction in cross-polarized light. The QS stage quartz veins are less deformed than the QM stage. Quartz veins in the QC stage are straightforward (Fig. 3K) and often display a druse or comb-like structure, indicating quartz growth in an open space environment. Four types of inclusion have been identified, based on their compositions and phases (L–V–S) at room temperature (Fig. 5). Phase transitions were observed during the heating and cooling process. Laser Raman spectroscopy, SEM photos and corresponding EDS spectra have been used to test the compositions of the fluid and daughter minerals hosted in quartz from different paragenetic stages.

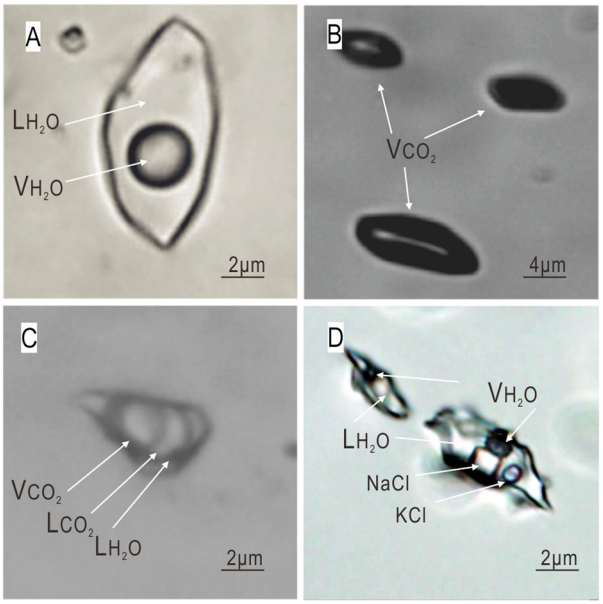

Figure 5. FIs types in the quartz veins from the Talate Pb–Zn(–Fe) deposit (plane-polarized light), **A**, aqueous FI (W-type) FIs in quartz vein in the QC stage; **B**, pure carbonic (PC-type) FIs in quartz vein in the QM stage; **C**, the carbonic type (C-type) FIs in quartz vein in the QS stage; **D**, the mineral-bearing or multiphase (S-type) FIs in quartz vein in the QM stage. This figure is available in colour online at wileyonlinelibrary.com/journal/gj

4.2.1. *Aqueous FIs (W-type)*

These are encountered in every stage (Fig. 5A). W-type FIs are two-phase (liquid and vapour H_2O) NaCl–H_2O systems, with the gas bubble making up approximately 20–30% of the entire volume in the QM stage, about 10–30% in the QS stage and 5–10% in the QC stage. The majority of FIs have irregular shapes with sizes ranging from 6 to 20 µm.

4.2.2. *Pure carbonic FIs (PC-type)*

These FIs are found in the QM and QS stages (Fig. 5B). PC-type FIs are one- or two-phase (liquid or/and vapour CO_2) carbonic system, with the gas bubble making up 50–90% in volume. They commonly show black, brown and brownish black colours, and the majority of FIs are long strips, or oval in shape with sizes ranging from 4 to 18 µm.

4.2.3. *The CO_2-rich FIs (C-type)*

This type of FI is found in the QM and QS stage quartz veins, in groups or as single inclusions (Fig. 5C). The C-type FIs are mostly two-phase (vapour CO_2 + liquid H_2O) or three-phase (vapour CO_2 + liquid CO_2 + liquid H_2O) with the gas phase ratio generally in the range of 40–70% at the start of the cooling process. They are generally triangular or elongate in shape, with sizes ranging from 5 to 38 µm.

4.2.4. *The daughter mineral-bearing FIs (S-type)*

These FIs are only present in the QM stage quartz veins and contain one or more daughter minerals (Fig. 5D). The daughter

minerals are cubic, round or irregular in shape. Generally, the cubic mineral is halite, and the round transparent mineral is mostly sylvite. The S-type FIs are generally between 5 and 20 μm.

4.3. Results

4.3.1. Microthermometry

Two hundred and ninety-six FIs in quartz crystals from multiple paragenetic stages were analysed, and their microthermometric results are presented in Table 1 and Figure 6. The quartz–magnetite stage contains all four types of FIs, i.e. W-type (46%), C-type (28%), S-type (22%) and PC-type (4%). The W-type FIs yielded homogeneous temperatures ranging from 271 to 426 °C, with freezing points (Tm_{ice}) between −20.0 to −0.8 °C that correspond to salinities of 1.4 to 22.4 wt.% NaCl eqv., and the densities range from 0.75 to 0.90 g/cm^3. In the C-type FIs, the melting temperatures of solid CO_2 (Tm_{CO2}) range from −60.0 to −56.7 °C, slightly below the triple-phase point (−56.6 °C) of CO_2, implying the presence of CH_4, which is consistent with the laser Raman spectrum results. The salinities range from 0.5 to 15.1 wt.% NaCl eqv. based on the clathrate melting temperatures (Tm_{clath}) of 0.4–9.8 °C, and the homogenizing temperatures of CO_2 (Th_{CO2}) are from 10.2 to 21.2 °C, corresponding to CO_2 densities are from 0.76 to 0.86 g/cm^3, with the density of C-type FIs ranging from 0.93 to 0.97 g/cm^3. The FIs completely homogenized between 272 and 347 °C ($Th_{\sim tal}$) with the majority going to vapour (85%) and a small number to liquid (about 12%). A few C-type FIs (3%) decrepitated before total homogenization in the heating process at temperatures of 390–426 °C. The S-type FIs completely homogenized at temperatures ranging between 288 to 424 °C with 67% going to vapour and the rest going to liquid (30%) or decrepitated in the heating process (about 3%). Usually, daughter minerals in the S-type FIs melted at between 182 to 420 °C during heating (Tm_S), indicating a salinity range of 31–41 wt.% NaCl eqv. PC-type FIs were dark brown in colour and failed to yield temperatures due to the single vapour phase. The QM stage also contains a small number of secondary W-type inclusions (approximately 3%), which have small bubbles accounting for about 5–10% in volume and are mostly distributed along the fissures, homogenized at temperatures of about 180 °C.

FIs in the quartz–sulphide (QS) stage are mainly W-type (55%) with 40% C-type inclusions and a small amount of PC-type FIs (5%). The final ice melting temperatures of W-type FIs range from −11.6 to −0.1 °C, corresponding to salinities of 0.2–15.6 wt.% NaCl eqv., with densities of 0.84–0.91 g/cm^3. When heated to 204–269 °C, most FIs homogenized to liquid. The initial melting temperatures of C-type FIs are around −59.0 to −56.8 °C, and the melting temperatures of clathrate are between 5.4 and 8.2 °C, with the salinities from 3.5 to 8.4 wt.% NaCl eqv. The CO_2 phase partially homogenized at 5.4–8.2 °C corresponding to a CO_2 phase density of 0.77–0.85 g/cm^3, and 0.91–0.95 g/cm^3 of the C-type FIs. The total homogenization temperatures range from 246 to 266 °C, with the FIs mainly homogenizing to liquid, although some FIs (~2%) decrepitated before homogenization.

FIs in the quartz–carbonates (QC) stage are mainly W-type and yielded final ice temperatures of −6.5 to −0.6 °C, corresponding to salinities of 1.1 to 9.9 wt.% NaCl eqv. and densities 0.90–0.94 g/cm^3. The FIs homogenized to liquid at temperatures of 175–211 °C.

4.3.2. Laser Raman spectroscopy analysis

The PC-type FIs contain CO_2 and small amounts of N_2 but no H_2O component (Fig. 7A and 7B). The main vapour components of the C-type FIs are CO_2, N_2, CH_4 and liquid dominated by H_2O (Fig. 7C–E). The W-type FIs contain relatively high intensity water peaks (Fig. 7F). Most of the vapour and liquid phase in the S-type FIs is H_2O, with a few containing CO_2; however, the Raman spectroscopy was not able to identify the transparent cube daughter minerals. Gaseous components of the FIs in the QM stage are complex and variable, with $CO_2 + H_2O \pm N_2 \pm CH_4$ most of which have distinct peaks, indicating a high vapour concentration (Fig. 7A–C). The vapour concentrations of the

Table 1. Microthermometric data of the fluid inclusions in quartz from the Talate Pb–Zn(–Fe) deposit

Stage	Type	N	Tm_{CO2} (°C)	Tm_{clath} (°C)	Th_{CO2} (°C)	Tm_{ice} (°C)	Tm_S (°C)	$Th_{\sim tal}$ (°C)	Salinity (wt.%NaCl)	Density (g/cm^3)
QM	C	44	−60.0 to −56.7	0.4–9.8	10.2–21.2	—	—	272–347	0.5–15.1	0.93–0.97
	S	35	—	—	—	—	182–420	288–424	31–41	—
	W	73	—	—	—	−20.0 to −0.8	—	271–426	1.4–22.4	0.75–0.90
	PC	6	—	—	—	—	—	—	—	—
QS	C	34	−59.0 to −56.8	5.4–8.2	12.1–20.4	—	—	246–266	3.5–8.4	0.84–0.91
	W	47	—	—	—	−11.6 to −0.1	—	204–269	0.2–15.6	0.77–0.85
	PC	4	—	—	—	/	—	—	—	—
QC	W	94	—	—	—	−6.5 to −0.6	—	175–211	1.1–9.9	0.90–0.94

Tm_{CO2} = melting temperature of CO_2; Tm_{clath} = final melting temperature of CO_2–H_2O clathrate; Th_{CO2} = partial homogenization temperature of CO_2; Tm_{ice} = final melting temperature of ice; Tm_S = final dissolution temperature of halite daughter crystal; $Th_{\sim tal}$ = total homogenization temperature.

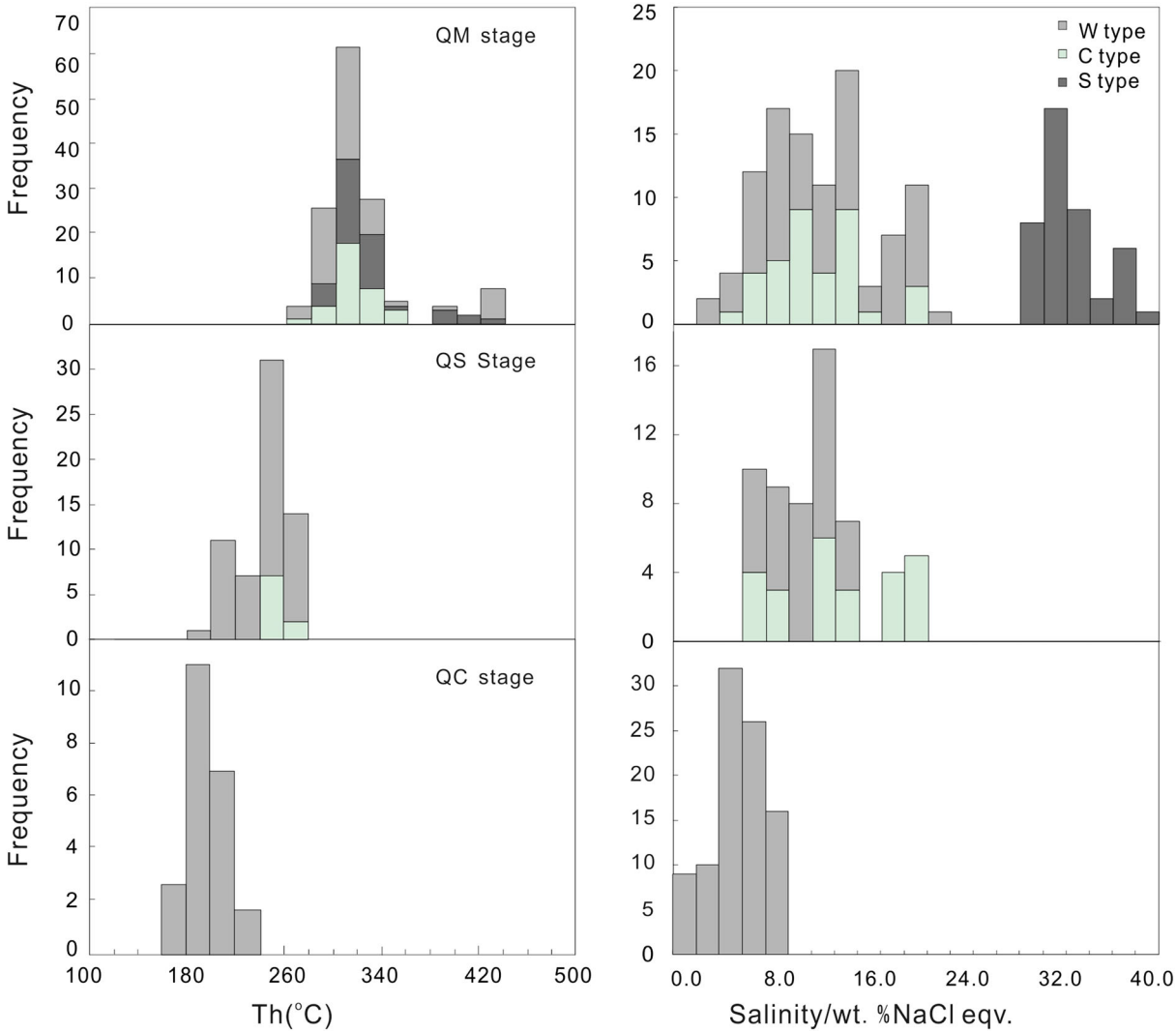

Figure 6. Histograms of homogenization temperatures and salinities of FIs in different stages in the Talate Pb–Zn(–Fe) deposit. This figure is available in colour online at wileyonlinelibrary.com/journal/gj

QS stage are lower and characterized by a strong water peak with multiple CO_2, CH_4 and N_2 peaks (Fig. 7D and 7E). The QC stage is dominated by water, with only a few showing a weak CO_2 peak (Fig. 7F).

4.3.3. SEM/EDS analysis of S-type fluid inclusions

The major daughter minerals in S-type FIs are generally halite, sylvite and pyrite with the halite mostly cubic in shape whereas the sylvite is commonly round (Fig. 8). The EDS spectra show that the (K + Na)/Cl has an atomic ratio of about 1:1 in sample 11TL-X, and above 1:1 in 11TL-44, which suggests that it contains other K-bearing minerals such as K-feldspar. The ratio for Fe and S are over 1:2 indicating that many contain not only pyrite (FeS_2) but also additional iron. The S-type FIs are metalliferous (Na, Al, K, Cr, Ca, Fe and/or Zn) and also contain anions such as Cl, S and O (Table 2). These elements indicate the presence of halite, sylvite or silicates, whereas Ca may indicate the existence of carbonate or wollastonite. The occurrence of a Zn peak in these samples indicates that the S-type inclusions likely host the ore-forming fluid.

5. SULPHUR ISOTOPE GEOCHEMISTRY

5.1. Samples and analytical methods

Six sulphide samples representing different mineralization stage were chosen. Sample 11TL-34 (pyrite) occurred with garnet (Fig. 3J); samples 11TL-12 (pyrite) and 11TL-15 (pyrite) of the QM stage occurred with magnetite; samples 11TL-21 (pyrite) and 11TL-43 (galena) occurred with sphalerite, galena and other sulphide minerals; and sample 11TL-11 (pyrite) occurred with calcite (Fig. 3L).

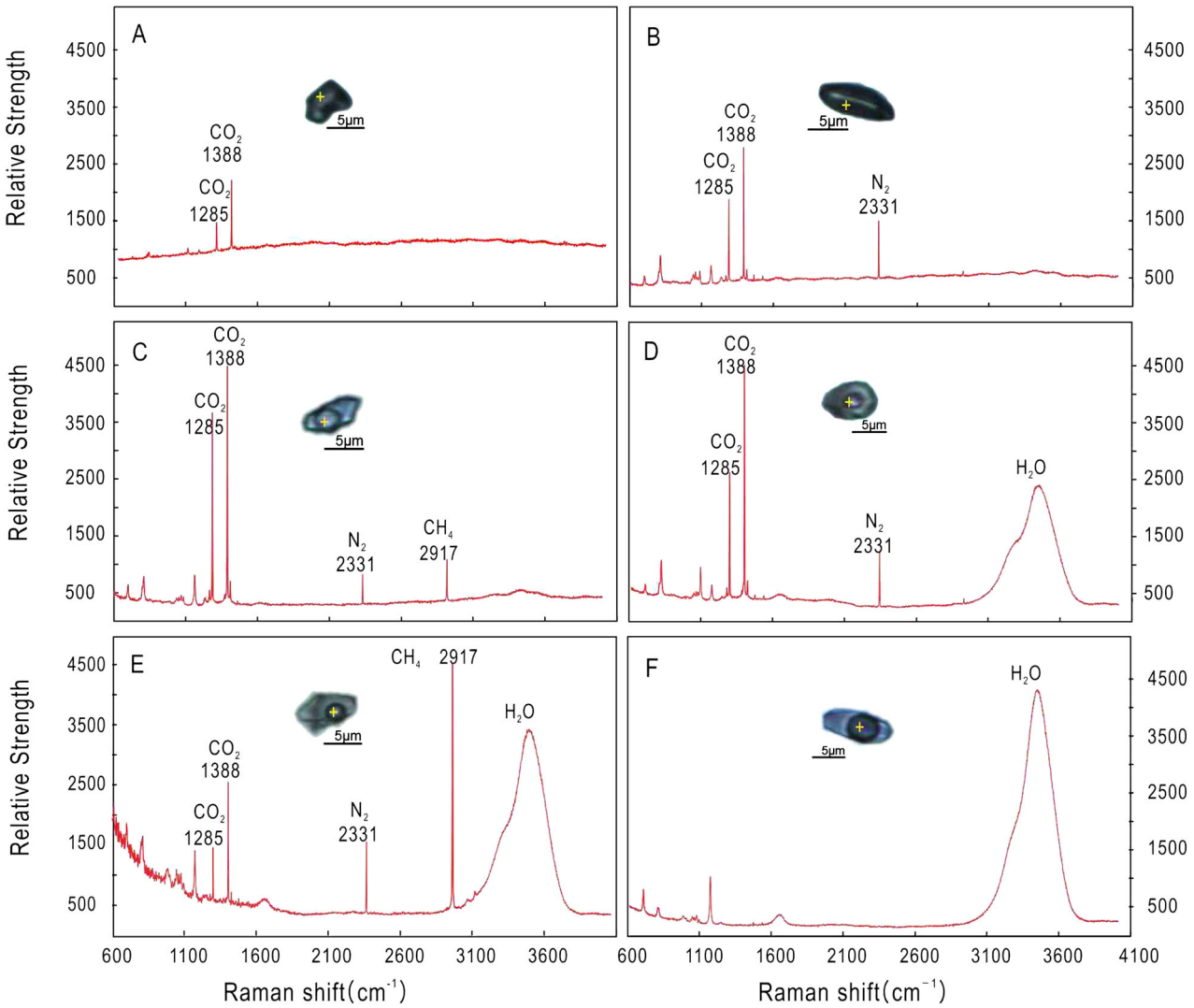

Figure 7. The LRM spectra of vapour component in FIs in the Talate Pb–Zn(–Fe) deposit, **A** and **B** show the PC-type FIs containing CO_2 and/or N_2, CH_4; **C**, **D** and **E** show the C-type FIs containing CO_2, H_2O and/or N_2; F, shows the W-type FIs only containing water peak. This figure is available in colour online at wileyonlinelibrary.com/journal/gj

Sulphur isotope analysis was carried out at the Analytical Laboratory of the Beijing Research Institute of Uranium Geology, China. Minerals were separated by crushing, sieving and handpicking down to a 250 μm fraction. Approximately 3–8 mg of sulphide was separated for analysis, and the purity of each sulphide sample was greater than 80% (in most cases >90%). Six sulphide samples were analysed by Delta v plus, with reproducibility of ±0.2‰ for $\delta^{34}S$ (1σ). Sulphur isotopes are reported as per mil (‰) deviations from the Vienna Cañon Diablo Troilite (V-CDT) standard.

5.2. *Results*

The $\delta^{34}S$ values for the six sulphide samples at Talate range from −7.4‰ to −1.7‰, with a mean of −4.6‰. Sample 11TL-34 from the E-skarn stage yielded a value of −7.4‰, whereas pyrite from samples 11TL-12 and 11TL-15 of the quartz–magnetite (QM) stage yielded values of −4.8‰ and −5.0‰, respectively. Pyrite in the quartz–sulphide (QS) stage yielded a value of −1.7‰ (11TL-21) and galena of −6.6‰ (11TL-43). The pyrite in the quartz–carbonate (QC) stage yielded a $\delta^{34}S$ value of −2.2‰ (Table 3).

Given the fO_2 and temperature during mineral precipitation, the total $\delta^{34}S$ values of hydrothermal fluids can be estimated from the $\delta^{34}S$ values of sulphides and sulphates (Ohmoto and Rye, 1979; Ohmoto and Goldhaber, 1997). The magnetite–pyrite buffer (Ohmoto and Rye, 1979) was used in both the E-skarn and QM stages, because magnetite coexists with pyrite in those two stages. The temperatures determined from microthermometry range

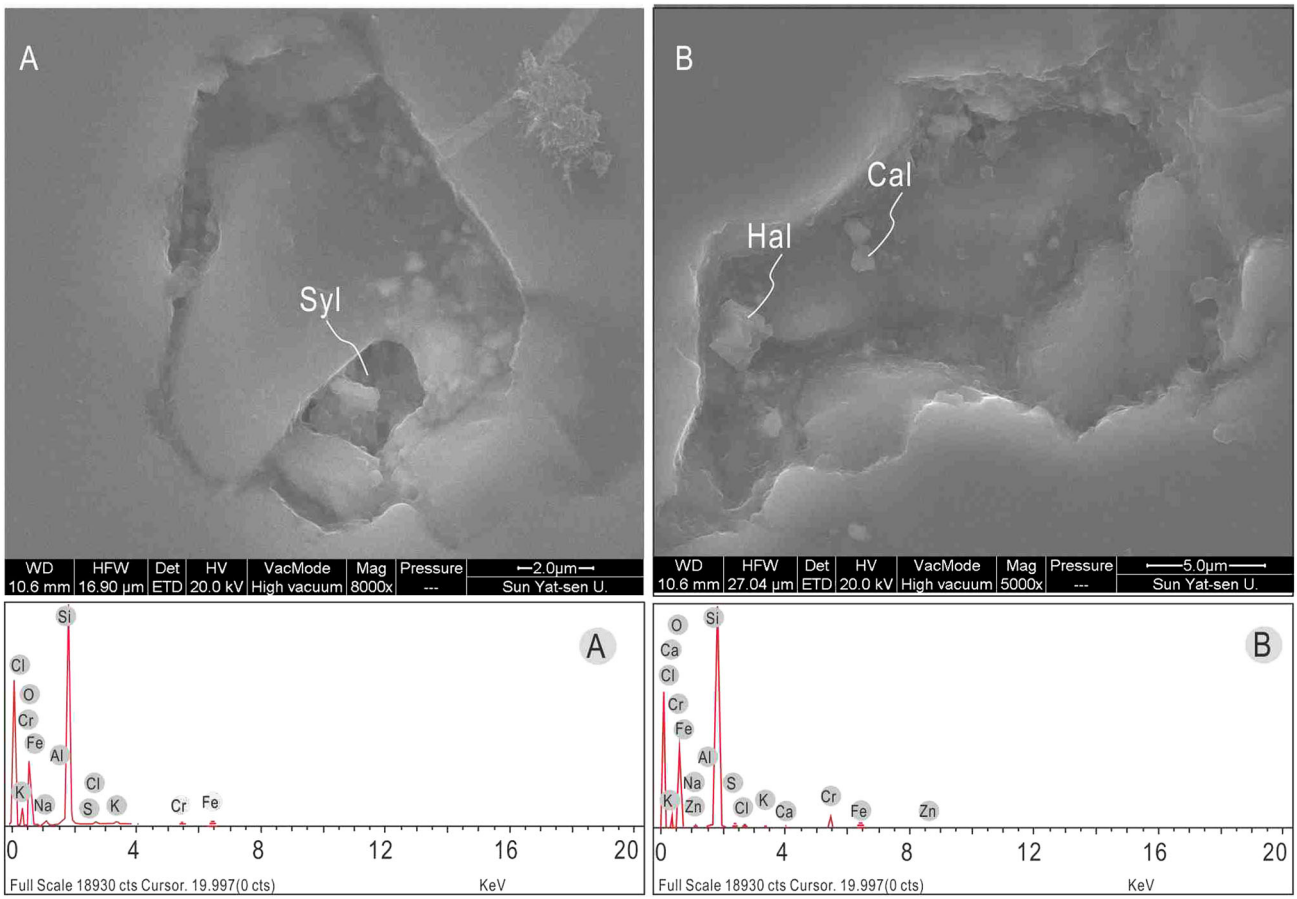

Figure 8. SEM photos and corresponding EDS spectra of daughter minerals in S-type fluid inclusions. This figure is available in colour online at wileyonlinelibrary.com/journal/gj

Table 2. The EDS results of daughter minerals in S-type FIs in the Talate Pb–Zn(–Fe) deposit

Sample	Element	O	Na	Al	Si	S	Cl	K	Cr	Fe	Zn	Ca	Total
11TL-X	Wt.%	44.99	0.79	0.19	37.47	1.24	0.97	0.44	8.54	1.01	4.22	0.12	100
	Atom%	62.28	0.76	0.16	29.55	0.86	0.6	0.25	3.64	0.4	1.43	0.07	
11TL-44	Wt.%	46.59	0.83	0.41	43.84	0.21	0.76	0.85	1.75	4.77			100
	Atom%	62.05	0.77	0.32	33.26	0.14	0.45	0.46	0.72	1.82			

Table 3. The sulphide isotope compositions of the Talate Pb–Zn(–Fe) deposit

Sample	Stage	Mineral	$\delta^{34}S$	T (°C)	fO_2 indicator	$\Delta = \delta^{34}S_{H2S} - \delta^{34}S_{fluid}$	$\delta^{34}S_{fluid}$
11TL-34	E-Skarn	Pyrite	−7.4‰	>350	Mt–Py	~10.0‰	2.6‰
11TL-12	QM	Pyrite	−4.8‰	350	Mt–Py	~10.0‰	5.2‰
11TL-15	QM	Pyrite	−5.0‰	350	Mt–Py	~10.0‰	5.0‰
11TL-21	QS	Pyrite	−1.7‰	250	Py–Po	0.0	−1.7‰
11TL-43	QS	Galena	−6.6‰	250	Py–Po	0.0	−6.6‰
11TL-11	QC	Pyrite	−2.2‰	200	Py–Po	0.0	−2.2‰

from 271 to 426 °C, indicating that the $\delta^{34}S$ values of the fluids were likely around +10‰ higher than those of sulphides (Table 3; Ohmoto and Goldhaber, 1997). In the main Pb–Zn mineralization (i.e. quartz–sulphide) stage, pyrrhotite coexists with chalcopyrite, and the magnetite was partly replaced by the pyrrhotite and chalcopyrite (Fig. 3J),

which suggests a relatively reduced environment (i.e. the pyrite–pyrrhotite buffer defined by Ohmoto and Rye (1979)), and the difference between the $\delta^{34}S$ values of sulphide and fluids ($\Delta = \delta^{34}S_{H2S} - \delta^{34}S_{fluid}$) would therefore be negligible (Ohmoto and Rye, 1979). Only pyrite occurred in the QC stage, and the $\delta^{34}S$ values of sulphide were likely similar to the fluids.

6. BIOTITE ^{40}AR/^{39}AR GEOCHRONOLOGY

6.1. Sample and methodology

Two biotite samples were selected from the QM and QS stages. Sample 11TL-53 from the QM stage comprises brecciated quartz with magnetite and rare sulphides, whereas sample 11TL-10 of QS stage contains abundant sulphides with small amounts of less deformed quartz (Fig. 3D and I).

An EPMA (electron-probe micro analyser), at the Electron Probe Laboratory of Guangzhou Institute of Geochemistry, Chinese Academy of Sciences, was used to determine the mica type and chemical composition with the detailed methodology and experimental parameters given in Huang *et al*. (2007).

Step-heating ^{40}Ar/^{39}Ar measurements were carried out using the MM-1200 and GV Instruments 5400 mass spectrometer at the Ar–Ar Laboratory of Guangzhou Institute of Geochemistry, Chinese Academy of Sciences, following the analytical procedures of Qiu and Wijbrans (2008). The biotite separates, together with the monitor standard DRA1 sanidine with an assumed age of 25.26 ± 0.07 Ma, wrapped in aluminium foil and shielded with cadmium foil, were irradiated with fast neutrons for 54 h at the Chinese Academy of Nuclear Energy Sciences, Beijing. Correction factors for interfering argon isotopes derived from Ca and K are $(^{39}Ar/^{37}Ar)_{Ca} = 8.984 \times 10^{-4}$, $(^{36}Ar/^{37}Ar)_{Ca} = 2.673 \times 10^{-4}$ and $(^{40}Ar/^{39}Ar)_{K} = 5.97 \times 10^{-3}$. The sample was crushed in a 210 × 28 mm (in bore diameter) high-temperature resistant stainless steel tube (T_{max} is 1200 °C). The extraction and purification lines were baked out for about 10 h at 150 °C using a heating tape and the crusher at 250 °C using an external tube furnace. The blanks are ^{36}Ar (0.002–0.004) mV, ^{37}Ar (0.0002–0.0006) mV, ^{38}Ar (0.0004–0.0015) mV, ^{39}Ar (0.0025–0.0051) mV and ^{40}Ar (0.51–1.3) mV. The released gas was purified for 5–8 min by two Zr/Al getter pumps operating at room temperature and ~450 °C. The ^{40}Ar/^{39}Ar results were calculated and plotted using the ArArCALC software (Koppers, 2002). Plateau, isochron and inverse isochron ages are given at 2σ confidence level. The uncertainties on the ^{40}Ar/^{39}Ar ratios of the monitors are included in the calculation of the integrated and plateau age uncertainties, but the error on the age of the monitor is not included.

6.2. Results

The mica type and calculated molecular formula are shown in Table 4. Their oxide contents imply that they are biotite (Deer *et al*., 1997) with formula being $(K_{1.07}, Na_{0.01})_{1.08}\{(Fe_{1.48}, Mg_{1.24}, Mn_{0.07}, Al_{0.06}, Ti_{0.06}, Cr_{0.01})_{2.92}[(Al_{1.09}, Si_{2.91})_4O_{10}](OH)_2\}$ for sample 11TL-53 and $(K_{0.87}, Na_{0.12})_{0.99}\{(Mg_{1.61}, Fe_{0.99}, Al_{0.32}, Ti_{0.05}, Mn_{0.03}, Cr_{0.01})_{3.01}[(Al_{1.05}, Si_{2.95})_4O_{10}](OH)_2\}$ for sample 11TL-10.

The geochronology results are shown in Table 5 and Figure 9. Sample 11TL-53 yielded a 27-step age spectrum with a plateau age of 227.6 ± 2.2 Ma (2σ), which covered as many as 21 heating stages, whereas sample 11TL-10 yielded a 20-step plateau age of 214.1 ± 2.1 Ma (2σ), which comprised 18 heating stages. The isochron and inverse isochron ages are 228.3 ± 2.3 and 213.7 ± 2.1 Ma, and their MSWD are 3.0 and 2.5, respectively (Fig. 9). The initial ^{40}Ar/^{36}Ar values of isochron ages are 289.7 ± 4.8 and 299.2 ± 5.4 Ma, and the inverse isochron ages are 289.4 ± 5.3 and 290.0 ± 4.9 Ma. All values are consistent with the atmospheric value (295.5 Ma) within the analytical error, suggesting the ^{40}Ar/^{39}Ar analysis is reliable.

7. DISCUSSION

7.1. Sources of sulphide

The $\delta^{34}S$ values of pyrite from the E-skarn and QM stage are between −4.8‰ and −7.4‰; however, the sulphur isotope values of fluids (ΣS_{fluid}) range from 2.6‰ to 5.2‰ (Table 3). In a system in equilibrium, it is the $\delta^{34}S\Sigma S_{fluid}$ value that should be used to estimate the source of sulphur (Ohmoto and Goldhaber, 1997). The $\delta^{34}S$ value of fluids in the E-skarn stage (2.6‰) is close to those of magmatic-

Table 4. The composition (%, by EPMA) and molecular formula of biotite coexisting with magnetite (11TL-53) and pyrite (11TL-10)

Sample	Na_2O	TiO_2	Al_2O_3	K_2O	SiO_2	Cr_2O_3	MgO	CaO	MnO	FeO	NiO	Total
11TL-53	0.05	0.92	11.54	9.93	34.26	0.20	9.80	—	0.93	20.83	—	88.46
11TL-10	0.80	0.81	15.21	8.93	38.61	0.09	14.18	0.03	0.50	15.53	—	94.70
11TL-53	$(K_{1.07}, Na_{0.01})_{1.08}\{(Fe_{1.48}, Mg_{1.24}, Mn_{0.07}, Al_{0.06}, Ti_{0.06}, Cr_{0.01})_{2.92}[(Al_{1.09}, Si_{2.91})_4O_{10}](OH)_2\}$											
11TL-10	$(K_{0.87}, Na_{0.12})_{0.99}\{(Mg_{1.61}, Fe_{0.99}, Al_{0.32}, Ti_{0.05}, Mn_{0.03}, Cr_{0.01})_{3.01}[(Al_{1.05}, Si_{2.95})_4O_{10}](OH)_2\}$											

Table 5. $^{39}Ar/^{40}Ar$ results by stepwise laser ablation dating of biotite

No	$^{36}Ar(a)$	$^{37}Ar(Ca)$	$^{38}Ar(Cl)$	$^{39}Ar(K)$	$^{40}Ar(r)$	Age(Ma)	$^{40}Ar(r)$ %	$^{39}Ar(K)$ %
				11TL-53				
1	0.000323	0.000000	0.000022	0.003720	0.096001	224.12 ± 4.55	50.13	1.56
2	0.000271	0.000000	0.000028	0.005326	0.139298	226.97 ± 4.31	63.52	2.23
3	0.000041	0.000000	0.000006	0.001229	0.031387	221.99 ± 5.63	72.22	0.52
4	0.000765	0.000000	0.000091	0.015684	0.404715	224.12 ± 2.18	64.14	6.58
5	0.000387	0.000000	0.000021	0.003556	0.090464	221.16 ± 5.13	44.18	1.49
6	0.000261	0.000000	0.000032	0.005029	0.128994	222.85 ± 2.79	62.58	2.11
7	0.000388	0.000000	0.000047	0.008935	0.232926	226.29 ± 2.06	66.98	3.75
8	0.000590	0.000000	0.000093	0.017095	0.452658	229.62 ± 1.75	72.20	7.17
9	0.000492	0.000000	0.000129	0.024196	0.640157	229.45 ± 1.39	81.48	10.15
10	0.000467	0.000000	0.000108	0.018245	0.478238	227.45 ± 1.42	77.59	7.65
11	0.000109	0.000000	0.000042	0.006412	0.168076	227.47 ± 1.64	83.92	2.69
12	0.000054	0.000000	0.000027	0.004457	0.116168	226.23 ± 1.81	87.98	1.87
13	0.000022	0.000000	0.000020	0.003395	0.089419	228.48 ± 1.96	93.06	1.42
14	0.000093	0.000000	0.000040	0.006580	0.172182	227.09 ± 1.72	86.26	2.76
15	0.000066	0.000000	0.000028	0.004721	0.124519	228.80 ± 1.66	86.41	1.98
16	0.000103	0.000000	0.000040	0.006950	0.181985	227.24 ± 2.06	85.64	2.91
17	0.000212	0.000000	0.000084	0.013241	0.347992	228.02 ± 1.19	84.72	5.55
18	0.000081	0.000000	0.000058	0.009644	0.252230	226.98 ± 1.23	91.27	4.04
19	0.000066	0.000000	0.000084	0.012968	0.342042	228.78 ± 1.16	94.55	5.44
20	0.000129	0.000000	0.000175	0.026182	0.682687	226.33 ± 0.92	94.68	10.98
21	0.000065	0.000000	0.000214	0.030087	0.793279	228.70 ± 0.92	97.62	12.62
				11TL-10				
1	0.001099	0.000000	0.000009	0.004773	0.117536	213.72 ± 9.96	26.58	2.09
2	0.000714	0.000000	0.000015	0.006945	0.171903	214.76 ± 4.30	44.89	3.04
3	0.000264	0.000000	0.000017	0.009121	0.226958	215.84 ± 1.70	74.38	4.00
4	0.000169	0.000000	0.000026	0.017458	0.433196	215.27 ± 0.99	89.67	7.65
5	0.000087	0.000000	0.000039	0.024227	0.598888	214.51 ± 0.96	95.84	10.61
6	0.000034	0.000000	0.000031	0.020995	0.518282	214.22 ± 0.90	98.06	9.20
7	0.000030	0.000000	0.000031	0.021009	0.519781	214.67 ± 0.92	98.32	9.20
8	0.000024	0.000000	0.000028	0.019326	0.475234	213.45 ± 0.93	98.50	8.46
9	0.000014	0.000000	0.000019	0.014506	0.357240	213.74 ± 0.98	98.86	6.35
10	0.000014	0.000000	0.000018	0.012407	0.304107	212.80 ± 0.98	98.59	5.43
11	0.000025	0.000000	0.000028	0.020725	0.510612	213.83 ± 0.87	98.54	9.08
12	0.000021	0.000000	0.000022	0.015858	0.390332	213.64 ± 0.92	98.42	6.95
13	0.000010	0.000000	0.000010	0.007737	0.192010	215.29 ± 1.13	98.51	3.39
14	0.000013	0.000000	0.000010	0.007663	0.190168	215.28 ± 1.65	97.97	3.36
15	0.000020	0.000000	0.000014	0.010484	0.256929	212.76 ± 1.38	97.67	4.59
16	0.000012	0.000000	0.000008	0.006218	0.152140	212.45 ± 1.28	97.68	2.72
17	0.000013	0.000000	0.000006	0.005171	0.128543	215.62 ± 1.77	97.05	2.27
18	0.000004	0.000000	0.000000	0.001157	0.028766	215.59 ± 9.83	95.99	0.51

hydrothermal fluids (i.e. around 0‰; Hoefs, 2009). However, $\delta^{34}S$ values in the quartz–magnetite stage (5–5.2‰) are slightly higher than those of both magmatic-hydrothermal and skarn stage fluids, which suggests addition of a heavier sulphur isotope fluid in the quartz–magnetite stage, consistent with the marble and metasedimentary host rocks that can contain heavy sulphur isotopes formed during evaporation (Hoefs, 2009). Fluids formed through reaction between the early skarn magmatic-hydrothermal fluids and the host rocks likely entered the system in the quartz–magnetite stage and generated the magnetite and associated 'hydro-skarn' minerals (Fig. 3E).

In the quartz–sulphide stage (i.e. the main mineralization stage), both pyrite and $\delta^{34}S\Sigma S_{fluid}$ values (−1.7‰) are close to those of magmatic-hydrothermal fluids (Table 3); however, these values are lower than those of quartz–magnetite stage (5–5.2‰). Based on the mineral assemblage and fluid inclusion studies, significant reduction occurred during the transition from the quartz–magnetite to the quartz–sulphide stage, probably accompanied by escape of H_2S during fluid boiling (see discussion below). Such processes would result in an increase of $\delta^{34}S$ values in the ore-forming fluids (Ohmoto and Goldhaber, 1997), so that the $\delta^{34}S$ values of the QS stage fluids should be higher than 5‰ if this is a continuous hydrothermal system derived from the early

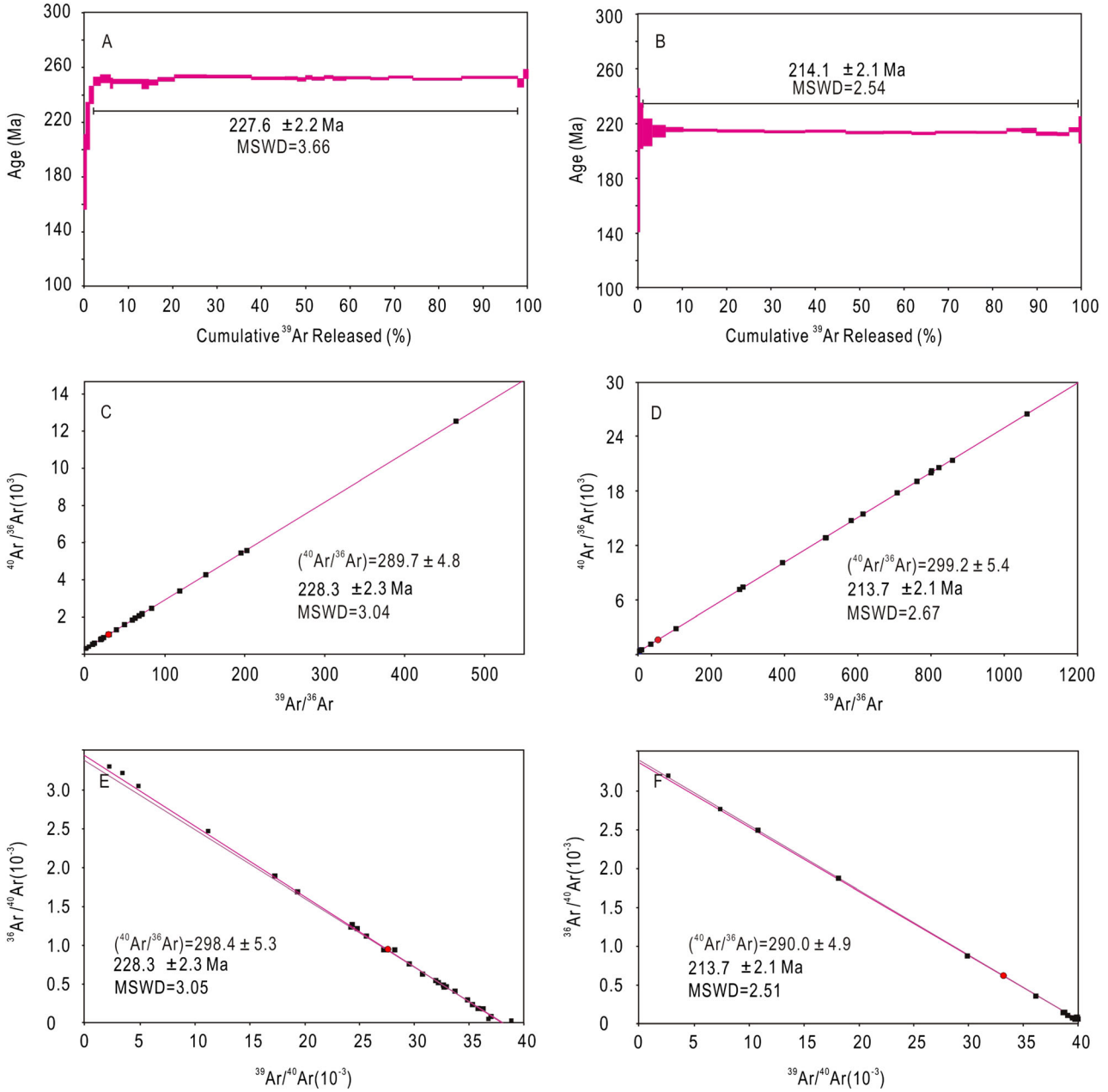

Figure 9. ^{40}Ar/^{39}Ar plateau (**A**, **B**), isochron (**C**, **D**) and inverse isochron (**E**, **F**) ages for biotite at Talate. This figure is available in colour online at wileyonlinelibrary.com/journal/gj

quartz–magnetite stage. The low δ^{34}S value of the quartz–sulphide stage (−1.7‰) indicates that the main mineralization stage at Talate may not be directly associated with the E-skarn and QM stage, though it is probably dominated by magmatic-hydrothermal fluids. This is consistent with the Ar–Ar dating of biotite from quartz–magnetite and quartz–sulphide stage.

7.2. *Fluid boiling and P–T conditions*

Numerous studies show that fluid boiling is able to accelerate mineral precipitation (Roedder, 1971; Roedder and Bodnar, 1980; Sato, 1980; Chen and Wang, 2011; Li *et al*., 2011, 2012a, 2012b; Yang *et al*., 2012; Zhang *et al*., 2012; Zheng *et al*., 2012; Deng *et al*., 2013). The combination of W-, C- and PC-type FIs in the quartz–sulphide (main mineralization) stage with significantly different vapour/liquid ratios in the same section (Fig. 11) and similar homogenization temperatures for the different phrases (Table 1) indicates that the ore fluid has probably gone through boiling (Lu *et al*., 2004). During this process, the homogenization temperature and pressure of analysed fluid inclusions will be equal to those of the trapping

conditions (Roedder and Bodnar, 1980). Using the homogenization temperatures, homogenization behaviours and proportion of the CO_2 phase in the C-type inclusions, the density and pressure of the FIs were calculated using the FLINCOR program (Brown, 1989). The trapping pressure of the QS stage ranges from 107 to 171 MPa (Fig. 10). Based on the approximate rock density (2.8 g/cm^3) and lithostatic pressure (28 MPa/km), the estimated depth of formation of the quartz–sulphide stage is 4–6 km, which is similar to many magmatic-hydrothermal systems in the East Qinling-Dabie area, including the porphyry Mo deposit at Yuchiling (Li *et al.*, 2012b); Jinduicheng (Yang *et al.*, 2009); Nannihu (Yang *et al.*, 2012), Shangfanggou (Yang *et al.*, 2013a), Zhaiwa (Deng *et al.*, 2013), Tangjiaping (Y. Wang *et al.*, 2009; Chen and Wang, 2011) and Qianechong (Yang *et al.*, 2013b), as well as the Sandaozhuang skarn Mo–W deposit (Shi *et al.*, 2009) and Qiyugou breccia pipe Au deposit (Li *et al.*, 2012a).

7.3. *Evolution of the ore-forming fluids*

Fluids in the QM stage are characterized by high temperatures, high salinities and CO_2-rich (Fig. 11A), with an estimated minimum pressure of 124–232 MPa. This fluid, which is probably S^{2-} unsaturated, is unfavourable for sulphide deposition, consistent with the precipitation of abundant magnetite, but limited sulphide, during the QM stage. Reaction between hydrothermal fluids and the host sedimentary rocks may have occurred during the QM stage, and the CO_2-rich fluids would have been involved in the ore-forming system and led to the precipitation of quartz and magnetite that are associated with hydro-skarn minerals.

In the QS stage, the homogenization temperatures, salinities, trapping pressures and CO_2 contents of FIs (Fig. 11B) are lower than those in quartz–magnetite stage. This decrease could be the result of either continuous evolution of QM stage fluids or represent a separate magmatic-hydrothermal system. The S isotope data and Ar–Ar dating are consistent with a separate system. These changes may trigger fluid boiling and facilitate the precipitation of sulphides, biotite alteration and the formation of quartz–sulphide stockworks in the main mineralization stage. Fluids associated with the quartz–carbonate stage are low-temperature, low-salinity and CO_2-depleted, comparable to meteoric water, likely representing the final stage of the Talate hydrothermal system.

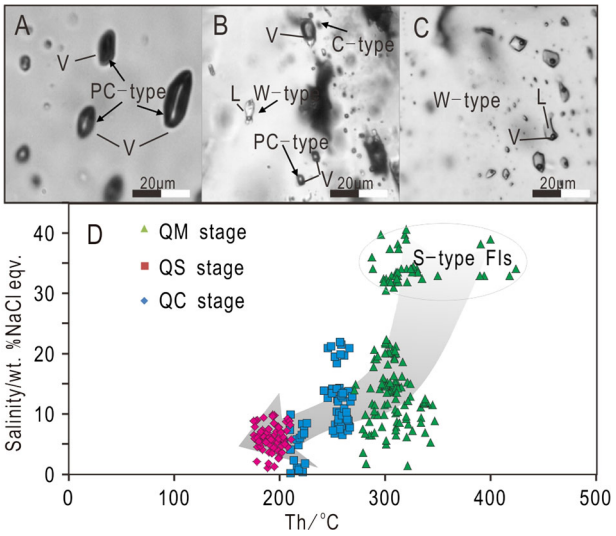

Figure 11. The evolution of ore-forming fluids in the Talate Pb–Zn(–Fe) deposit A, vapour-rich fluid inclusions (FIs) in QM stage, B, vapour-rich FIs coexist with liquid-rich FIs in QS stage, C, liquid-rich FIs in QC stage, D, evolution of temperature and salinity from QM to QC stage. L—liquid phase, V—vapour phase. This figure is available in colour online at wileyonlinelibrary.com/journal/gj

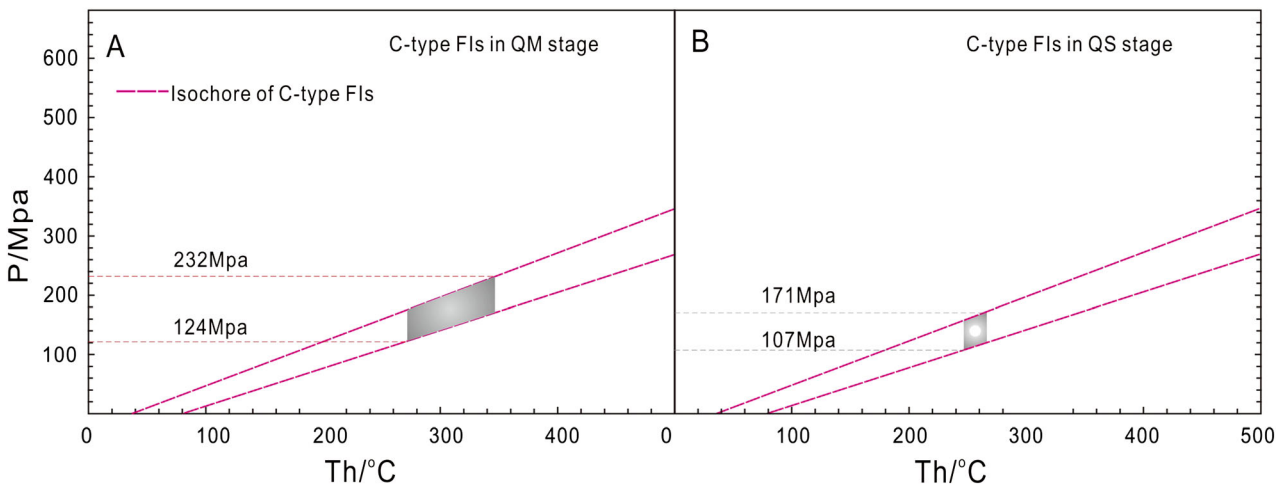

Figure 10. Diagram showing the estimated trapping pressure for the Talate Pb–Zn(–Fe) deposit. Isochors of the C-type fluid inclusions are calculated using the FLINCOR software (Brown, 1989). This figure is available in colour online at wileyonlinelibrary.com/journal/gj

7.4. *Significance of the biotite $^{40}Ar/^{39}Ar$ dating*

The closure temperature for the Ar diffusion system of biotite is between 350 and 387 °C (Harrison *et al*., 1985). The average temperatures in the QM and QS stage fluids are below the closure temperature, indicating that the $^{40}Ar/^{39}Ar$ isotopic ages of biotite likely represent the age of mineralization.

The coincident plateau and isochron ages are interpreted to represent the actual time of ore formation after systematic error corrections, and the two ages likely represent two geological events. As shown in Figure 3D, biotite in sample 11TL-53 of the QM stage is hosted in the quartz breccia, and the mineral assemblage includes magnetite, quartz and garnet (part of the E-skarn stage). Quartz in sample 11TL-10 of the QS stage coexists with pyrite and galena and shows strong fragmentation and deformation that is quite different from the QM stage in its appearance and mineral assemblage (Fig. 3I). These differences are also supported by fluid inclusion and sulphur isotope evidence. The $^{40}Ar/^{39}Ar$ plateau ages of the QM and QS stages are 227.6 ± 2.2 and 214.1 ± 2.1 Ma, respectively, which indicates the quartz–magnetite stage formed 13 m.y. before the main mineralization quartz–sulphide stage. The 214.1 Ma age represents the formation age of the Talate Pb–Zn(–Fe) deposit and suggests that the Pb–Zn mineralization at Talate is distinct from the E-skarn and the QM stage.

7.5. *Ore deposit type and tectonic implications*

At Talate, sulphur isotope data indicate that the early magmatic-hydrothermal fluids interacted with the carbonate rocks in the Kangbutiebao Formation of Kelan Basin. The interaction between fluids and host rocks is limited to a few centimetres, and skarn alteration usually occurs as veins (Fig. 3K). Some anhydrous minerals including garnet and diopside formed in the E-skarn stage (Figs 3A–C and 4), whereas during the retrograde phase, magnetite and hydrous minerals such as epidote, tremolite, actinolite, hornblende and tourmaline precipitated together with quartz. Fluids associated with the QM stage is characterized by high temperatures, high salinities and CO_2-rich and is distinct from typical syngenetic deposits, such as VMS deposits which have a close relationship in space and time with the coeval volcanism (Oen, 1987; Schulz *et al*., 2002; Gu *et al*., 2003, 2004). This is consistent with the $^{40}Ar/^{39}Ar$ plateau age of biotite intergrown with quartz in the QM stage which yielded a younger age (227.6 ± 2.2 Ma) than the Kangbutiebao Formation (413–407 Ma; Chai *et al*., 2009). The distinct sulphur isotope values indicate that the main mineralization stage at Talate is not directly associated with the E-skarn and the QM stage. This is supported by the younger biotite ^{40}Ar–^{39}Ar plateau age of the QS stage (214.1 ± 2.1 Ma). The cumulative evidence suggests that the Talate Pb–Zn(–Fe) deposit is probably a separate magmatic-hydrothermal deposit only partially associated with skarn alteration.

New research shows that the southern edge of Altay has experienced Palaeo-Asian Ocean closure, arc-continent and continental–continental collision from the Permian to Triassic, with the most intense period in the Late Permian to Triassic (Xiao *et al*., 2009; Chen *et al*., 2012). During this time, granitic magmatism and metamorphism occurred together with polymetallic mineralization (Chen *et al*., 2006; Hu *et al*., 2006; Zheng *et al*., 2007), represented by granitoids such as the Lamazhao I-type to A-type granites (276 ± 9 Ma; Wang *et al*., 2005), the Taerlang amphibolitic and gabbroic rocks (266.9 ± 6.1 Ma; Cai *et al*., 2007), the Bukesala biotite monzogranite (277.0 ± 2.4 Ma; Gao *et al*., 2010) and the Shangkelan granite (220 Ma; T. Wang *et al*., 2009); metamorphosed rocks such as the Qinghe gneiss (281 ± 3 Ma; Hu *et al*., 2006), the Altay andalusite and sillimanite (268–261 Ma; Zheng *et al*., 2007), the Fuyun granulites (268–279 Ma; Chen *et al*., 2006) and mineral deposits such as the Tiemurte Pb–Zn (239.7 ± 2.4 and 235.2 ± 2.5 Ma; Zhang *et al*., 2012; Zheng *et al*., 2013), the Wulasigou copper deposit (219.8 ± 2.3 Ma; Zheng *et al*., 2012), the Sarekuobu Au deposit (213.5 ± 2.3 Ma; Zhang *et al*., 2014) and the Talate Pb–Zn(–Fe) deposit (214.1 ± 2.1 Ma and 227.6 ± 2.2 Ma). The Late Permian–Triassic continental collision is directly associated with regional metamorphism in the Altay area and resulted in a series of orogenic-type ore systems such as the Tiemurte Pb–Zn, Wulasigou Cu and Sarekuobu Au deposits (Zhang *et al*., 2012; Zheng *et al*., 2012; Zhang *et al*., 2014). Rapid igneous activity and associated deposit precipitation may be explained by the Late Palaeozoic post-orogenic extension after continental–continental collision (Zhou *et al*., 2004; Chen and Arakawa, 2005). Such magmatism is typically characterized by multiple stages and generates a range of hydrothermal alteration and mineralization, such as the 227 Ma quartz–magnetite alteration and 214 Ma Pb–Zn sulphide mineralization which are both associated with magmatic-hydrothermal fluids.

8. CONCLUDING REMARKS

Four mineralization stages can be identified in the Talate deposit: early skarn, late skarn with quartz–magnetite, quartz–sulphide and quartz–carbonate stage. Four types of FIs (W-, C-, S- and PC-type) have been observed in the quartz veins of the QM to QC stages. Evidence shows that original fluids in the QM stage are high-temperature, high-salinity and CO_2-rich and are distinct from the late QC stage fluids characterized by meteoric water. The QS main

mineralization stage is also CO_2-rich and went through boiling. The CO_2-rich fluids and high trapping pressures, together with much younger alteration and mineralization than that of the host rock, strongly suggest that Talate is not a seafloor hydrothermal exhalation system as described by previous studies in the Kelan Basin.

Evidence from sulphur isotopes indicate that both skarn and quartz–magnetite alteration and quartz–sulphide mineralization at Talate formed as a result of magmatic-hydrothermal fluids; however, mineralization may not be directly associated with the E-skarn and QM stages, which is consistent with the biotite $^{40}Ar/^{39}Ar$ plateau ages of 227.6 and 214.1 Ma from the QM and QS stages, respectively. This suggests that the Talate is an unusual skarn-type Pb–Zn(–Fe) deposit.

ACKNOWLEDGEMENTS

This study was supported by the Chinese National Basic Research 973-Program (2014CB440802, 2007CB411303) and the NSFC (nos. 41072062 and 40730421). The Office of Project-305 and Geological Team 706 of Xinjiang of Nonferrous Metals helped our field investigation. Discussions with Profs. Hongrui Fan, Jiuhua Xu and Dr Mei Mi, Nuo Li, Suwei Yue, Yong-Fei Yang and the two unknown constructive reviewers greatly improved the quality of this paper. This is contribution No. IS-1891 from GIGCAS.

REFERENCES

Baker, T., **Van Achterberg, E.**, **Ryan, C.G.**, **Lang, J.R. 2004**. Composition and evolution of ore fluids in a magmatic-hydrothermal skarn deposit. *Geology* **32**, 117–120.

Bodnar, R.J. 1993. Revised equation and table for determining the freezing point depression of H_2O–NaCl solutions. *Geochimica et Cosmochimica Acta* **57**, 683–684.

Brown, P.E. 1989. Flincor: a microcomputer program for the reduction and investigation of fluid inclusion data. *American Mineralogist* **74**, 1390–1393.

Cai, K.D., **Yuan, C.**, **Sun, M.**, **Xiao, W.J.**, **Chen, H.L.**, **Long, X.P.**, **Zhao, Y.J.**, **Li, J. 2007**. Geochemical characteristics and ^{40}Ar–^{39}Ar ages of the amphibolites and gabbros in Tarlang area: implications for tectonic evolution of the Chinese Altay. *Acta Petrologica Sinica* **23**, 877–888 (in Chinese with English abstract).

Cai, K.D., **Sun, M.**, **Yuan, C.**, **Long, X.P.**, **Xiao, W.J. 2011**. Geological framework and Palaeozoic tectonic history of the Chinese Altay, NW China: a review. *Russian Geology and Geophysics* **52**, 1619–1633.

Chai, F.M., **Mao, J.W.**, **Dong, L.H.**, **Yang, F.Q.**, **Liu, F.**, **Geng, X.X.**, **Zhang, Z.X. 2009**. Geochronology of metarhyolites from the Kangbutiebao Formation in the Kelang Basin, Altay Mountains, Xinjiang: implications for the tectonic evolution and metallogeny. *Gondwana Research* **16**, 189–200.

Chen, B., **Arakawa, Y. 2005**. Elemental and Nd–Sr isotopic geochemistry of granitoids from the West Junggar foldbelt (NW China), with implications for Phanerozoic continental growth. *Geochimica Et Cosmochimica Acta* **69**, 1307–1320.

Chen, B., **Jahn, B.M. 2002**. Geochemical and isotopic studies of the sedimentary and granitic rocks of the Altay orogen of northwest China and their tectonic implications. *Geological Magazine* **139**, 1–13.

Chen, Y.J., **Wang, Y. 2011**. Fluid inclusion study of the Tangjiaping Mo deposit, Dabie Shan, Henan Province: implications for the nature of the porphyry systems of post-collisional tectonic settings. *International Geology Review* **53**, 635–655.

Chen, H.Y., **Chen, Y.J.**, **Liu, Y.L. 2001**. Metallogenesis of the Ertix gold belt, Xinjiang and its relationship to Central Asia-type orogenesis. *Science in China Series D-Earth Sciences* **44**, 245–255.

Chen, H.L., **Yang, S.F.**, **Li, Z.L.**, **Yu, X.**, **Xiao, W.J.**, **Yuan, C.**, **Lin, X.**, **Li, J. 2006**. Zircon SHRIMP U–Pb chronology of Fuyun basic granulite and its tectonic significance in Altaid orogenic belt. *Acta Petrologica Sinica* **22**, 1351–1358 (in Chinese with English abstract).

Chen, Y.J., **Ni, P.**, **Fan, H.R.**, **Pirajno, F.**, **Lai, Y.**, **Su, W.C.**, **Zhang, H. 2007**. Diagnostic fluid inclusions of different types of hydrothermal gold deposits. *Acta Petrologica Sinica* **23**, 2085–2108.

Chen, Y.J., **Pirajno, F.**, **Wu, G.**, **Qi, J.P.**, **Xiong, X.L. 2012**. Epithermal deposits in North Xinjiang, NW China. *International Journal of Earth Sciences* **101**, 889–917.

Cheng, J.L., **Zhao, Y.X.**, **Liu, F.H. 2009**. Comments on mineralization and geochemistry of skarn ore deposits. *Contributions to Geology and Mineral Resources Research* **24**, 329–334.

Collins, P.L. 1979. Gas hydrates in CO_2-bearing fluid inclusions and the use of freezing data for estimation of salinity. *Economic Geology* **74**, 1435–1444.

Deer, W.A., **Howie, R.A.**, **Zussman, J. 1997**. *Rock-forming Minerals. 2B. Double-chain Silicates*. Geological Society: London; 1–764.

Deng, X.H., **Chen, Y.J.**, **Santosh, M.**, **Yao, J.M. 2013**. Genesis of the 1.76Ga Zhaiwa Mo–Cu and its link with the Xiong'er volcanics in the North China Craton: implications for accretionary growth along the margin of the Columbia supercontinent. *Precambrian Research* **227**, 337–348.

Einaudi, M.T., **Burt, D.M. 1982**. Introduction, terminology, classification, and composition of skarn deposits. *Economic Geology* **77**, 745–754.

El-Sharkawi, M., **Dearman, W.R. 1966**. Tin-bearing skarns from the north-west border of the Dartmoor granite, Devonshire, England. *Economic Geology* **61**, 362–369.

Forster, D.B., **Seccombe, P.K.**, **Phillips, D. 2004**. Controls on skarn mineralization and alteration at the Cadia deposits, New South Wales, Australia. *Economic Geology* **99**, 761–788.

Frezzotti, M.L., **Tecce, F.**, **Casagli, A. 2012**. Raman spectroscopy for fluid inclusion analysis. *Journal of Geochemical Exploration* **112**, 1–20.

Ganino, C., **Arndt, N.T.**, **Zhou, M.F.**, **Gaillard, F.**, **Chauvel, C. 2008**. Interaction of magma with sedimentary wall rock and magnetite ore genesis in the Panzhihua mafic intrusion, SW China. *Mineralium Deposita* **43**, 677–694.

Gao, F.P., **Zhou, G.**, **Lei, Y.X.**, **Wang, D.S.**, **Chen, J.X.**, **Zhang, H.F.**, **Wu, X.B.**, **Liu, G.R.**, **Zhao, Z.H. 2010**. Early Permian granite age and geochemical characteristics in Shaerbuleke of Xinjiang's Altay area and its geological significance. *Geological Bulletin of China* **29**, 1281–1293 (in Chinese with English abstract).

Goldfarb, R.J., **Mao, J.W.**, **Hart, C.**, **Wang, D.**, **Anderson, E.**, **Wang, Z. 2003**. Tectonic and metallogenic evolution of the Altay Shan, Northern Xinjiang Uygur Autonomous Region, northwestern China. In: *Tectonic Evolution and Metallogeny of the Chinese Altay and Tianshan*, Mao, J. W., Godlfarb, R.J., Seltmann, R., Wang, D.H., Xiao, W.J., Hart, C. (eds). International Association on the Genesis of Ore Deposits, Centre for Russian and Central Asian Mineral Studies. Natural History Museum: London; 17–30.

Gu, X.X., **Schulz, O.**, **Vavtar, F.**, **Liu, J.M.**, **Zheng, M.H. 2003**. Ore fabric characteristics and their genetic significance of the Woxi W–Sb–Au deposit, Hunan. *Mineral Deposits* **22**, 107–120.

Gu, X.X., **Liu, J.M.**, **Schulz, O.**, **Vavtar, F.**, **Zheng, M.H. 2004**. Syngenetic origin for the Woxi W–Sb–Au deposit in Hunan: evidence from trace elements and sulphur isotopes. *Chinese Journal of Geology* **39**, 424–439.

Harrison, T.M., **Duncan, I.**, **McDougall, I. 1985**. Diffusion of $^{40}Ar/^{39}Ar$ in biotite: temperature, pressure and compositional effects. *Geochimica et Cosmochimica Acta* **49**, 2461–2468.

Hoefs, J. 2009. *Stable Isotope Geochemistry*. Springer: Berlin; 1–214.

Hu, A.Q., **Wei, G.J.**, **Deng, W.F.**, **Chen, L.L. 2006**. SHRIMP zircon U–Pb dating and its significance for gneisses from the southwest area to Qinghe County in the Altay, China. *Acta Petrologica Sinica* **22**, 1–10 (in Chinese with English abstract).

Huang, X.L., **Xu, Y.G.**, **Lo, C.H.**, **Wang, R.C.**, **Lin, C.Y. 2007**. Exsolution lamellae in a clinopyroxene megacryst aggregate from Cenozoic basalt, Leizhou Peninsula, South China: petrography and chemical evolution. *Contributions to Mineralogy and Petrology* **154**, 691–705.

Jamtveit, B., **Andersen, T. 1993**. Contact metamorphism of layered shale–carbonate sequences in the Oslo Rift; III, the nature of skarn-forming fluids. *Economic Geology* **88**, 1830–1849.

Jiao, X.J., **Kang, J.C.**, **Zhang, L.C. 2006**. Geological features of sedimentary deposits in Maizi Basin in southern Altay Mountains and the exploring direction. *Contributions to Geology and Mineral Resources Research* **21**, 178–183.

Koppers, A.A. 2002. ArArCALC-software for $^{40}Ar/^{39}Ar$ age calculations. *Computers and Geosciences* **28**, 605–619.

Kroener, A., **Alexeiev, D.V.**, **Rojas, A.Y.**, **Hegner, E.**, **Wong, J.**, **Xia, X.**, **Belousova, E.**, **Mikolaichuk, A.V.**, **Seltmann, R.**, **Liu, D.**, **Kiselev, V. V. 2013**. Mesoproterozoic (Grenville-age) terranes in the Yrgyz North Tianshan: zircon ages and 634 Nd–Hf isotopic constraints on the origin and evolution of basement blocks in the 635 southern Central Asian Orogen. *Gondwana Research* **23**, 272–295.

Kunzmann, T. 1999. The aenigmatite–rhonite mineral group. *European Journal of Mineralogy* **11**, 743–756.

Li, J.X., **Jiang, J.**, **Hu, X.P.**, **Kang, J.C.**, **Yin, Y.Q. 2003**. Geological features and genesis of the Mengku iron deposit in the Fuyun, Xinjiang. *Xinjiang Geology* **21**, 307–311 (in Chinese with English abstract).

Li, N., **Chen, Y.J.**, **Ulrich, T.**, **Lai, Y. 2011**. Fluid inclusion study of the Wunugetu Cu–Mo deposit, Inner Mongolia, China. *Mineralium Deposita* **45**, 467–482.

Li, N., **Carranza, E.J.M.**, **Ni, Z.Y.**, **Guo, D.S. 2012a**. The CO_2-rich magmatic-hydrothermal fluid of the Qiyugou breccia pipe, Henan Province, China: implication for breccia genesis and gold mineralization. *Geochemistry: Exploration, Environment, Analysis* **12**, 147–160.

Li, N., **Ulrich, T.**, **Chen, Y.J.**, **Thomsen, T.B.**, **Pease, V.**, **Pirajno, F. 2012b**. Fluid evolution of the Yuchiling porphyry Mo deposit, East Qinling, China. *Ore Geology Reviews* **48**, 442–459.

Liu, F., **Li, Y.H.**, **Mao, J.W.**, **Yang, F.Q.**, **Chai, F.M.**, **Geng, X.X.**, **Yang, Z.X. 2008**. SHRIMP U–Pb ages of the Abagong Granites in the Altay Orogen and their geological implications. *Acta Geologica Sinica* **29**, 795–804 (in Chinese with English abstract).

Liu, X.J., **Liu, W.**, **Liu, L.J.**, **Shang, H.J.**, **Liu, G.R. 2011**. Genesis of the Sawusi lead-zinc deposit in the eastern Maizi volcanic-sedimentary Basin, southern Altay Mountains. *Acta Petrologica Sinica* **27**, 1810–1828 (in Chinese with English abstract).

Liu, X.J., **Liu, W.**, **Liu, L.J. 2012**. The generation of a stratiform skarn and volcanic exhalative Pb–Zn deposit (Sawusi) in the southern Chinese Altay Mountains: the constraints from petrography, mineral assemblage and chemistry. *Gondwana Research* **22**, 597–614.

Lu, H.Z., **Liu, Y.M.**, **Wang, C.L.**, **Xu, Y.Z.**, **Li, H.Q. 2003**. Mineralization and fluid inclusion study of the Shizhuyuan W–Sn–Bi–Mo–F skarn deposit, Hunan Province, China. *Economic Geology* **98**, 955–974.

Lu, H.Z., **Fan, H.R.**, **Ni, P.**, **Ou, G.X.**, **Shen, K.**, **Zhang, W.H. 2004**. *Fluid Inclusion*. Science Press: Beijing; 1–487 (in Chinese).

Meinert, L.D. 1983. Variability of skarn deposits: guides to exploration. In: *Revolution in the Earth Sciences*, Boardman, S.J. (ed.). Kendall-Hunt Publishing Company: Iowa; 301–316.

Meinert, L.D. 1992. Skarns and skarn deposits. *Geoscience Canada* **19**, 145–162.

Meinert, L.D., **Hefton, K.K.**, **Mayes, D.**, **Tasiran, I. 1997**. Geology, zonation, and fluid evolution of the Big Gossan Cu–Au skarn deposit, Ertsberg district, Irian Jaya. *Economic Geology* **92**, 509–534.

Oen, I. 1987. Rift-related igneous activity and metallogenesis in SW Bergslagen, Sweden. *Precambrian Research* **35**, 367–382.

Ohmoto, H., **Rye, R.O. 1979**. Isotopes of sulphur and carbon. In: *Geochemistry of Hydrothermal Ore Deposits*, Barnes, H.L. (ed.). Holt Rinehart and Winston: New York; 509–567.

Ohmoto, H., **Goldhaber, M.B. 1997**. Sulphur and carbon isotopes. In: *Geochemistry of Hydrothermal Ore Deposits*, Barnes, H.L. (ed.). Wiley: New York; 517–612.

O'Neill, J.M., **Klein, T.L.**, **Sims, P.K. 2002**. Metallogeny of a Palaeoproterozoic collisional orogen through time—the Great Falls tectonic zone, Montana and Idaho. *Geological Society of America Abstracts with Programs* **34**, 336.

Pan, Y., **Dong, P. 1999**. The Lower Changjiang (Yangzi/Yangtze River) metallogenic belt, east central China: intrusion- and wall rock-hosted Cu–Fe–Au, Mo, Zn, Pb, Ag deposits. *Ore Geology Reviews* **15**, 177–242.

Pirajno, F. 2009. Hydrothermal Processes and Mineral Systems. Springer: Berlin; 1–1250.

Qiu, H.N., **Wijbrans, J.R. 2008**. The Palaeozoic metamorphic history of the Central Orogenic Belt of China from $^{40}Ar/^{39}Ar$ geochronology of eclogite garnet fluid inclusions. *Earth and Planetary Science Letters* **268**, 501–514.

Roedder, E. 1971. Fluid inclusion studies on the porphyry-type ore deposits at Bingham, Utah, Butte, Montana, and Climax, Colorado. *Economic Geology* **66**, 98–118.

Roedder, E., **Bodnar, R. 1980**. Geologic pressure determinations from fluid inclusion studies. *Annual Review of Earth and Planetary Sciences* **8**, 263.

Romer, R., **Soler, A. 1995**. U–Pb age and lead isotopic characterization of Au-bearing skarn related to the Andorra granite (central Pyrenees, Spain). *Mineralium Deposita* **30**, 374–383.

Sato, K. 1980. Tungsten skarn deposit of the Fujigatani mine, southwest Japan. *Economic Geology* **75**, 1066–1082.

Schulz, O., **Vavtar, F.**, **Gu, X.X. 2002**. Stratiform Sb–W–Au–Lagerstätte Woxi in Hunan, China. *Erzmetall* **55**, 535–540.

Shelton, K.L. 1983. Composition and origin of ore-forming fluids in a carbonate–hosted porphyry copper and skarn deposit; a fluid inclusion and stable isotope study of Mines Gaspe, Quebec. *Economic Geology* **78**, 387–421.

Shi, Y.X., **Li, N.**, **Yang, Y. 2009**. Ore geology and fluid inclusion geochemistry of the Sandaozhuang Mo–W deposit in Luanchuan county, Henan province. *Acta Petrologica Sinica* **25**, 2575–2587 (in Chinese with English abstract).

Sibson, R.H., **Robert, F.**, **Poulsen, K.H. 1988**. High-angle reverse faults, fluid-pressure cycling, and mesothermal gold–quartz deposits. *Geology* **16**, 551–555.

Takeuchi, M. 1994. Changes in garnet chemistry show a progressive denudation of the source areas for Permian–Jurassic sandstones, southern Kitakami Terrane, Japan. *Sedimentary Geology* **93**, 85–105.

Vityk, M.O., **Bodnar, R.J.**, **Schmidt, C.S. 1994**. Fluid inclusions as tectonothermobarometers: relation between pressure-temperature history and reequilibration morphology during crustal thickening. *Geology* **22**, 731–734.

Wan, B., **Zhang, L.C.**, **Xiao, W.J. 2010**. Geological and geochemical characteristics and ore genesis of the Keketale VMS Pb–Zn deposit, Southern Altay Metallogenic Belt, NW China. *Ore Geology Reviews* **37**, 114–126.

Wan, B., **Xiao, W.J.**, **Zhang, L.C.**, **Windley, B.F.**, **Han, C.M.**, **Quinn, C.D. 2011**. Contrasting styles of mineralization in the Chinese Altay and East Junggar, NW China: implications for the accretionary history of the southern Altaids. *Journal of the Geological Society* **168**, 1311–1321.

Wang, J.B., **Qin, K.Z.**, **Wu, Z.L.**, **Hu, J.H.**, **Deng, J.N. 1998**. *Volcanic-exhalative-sedimentary Lead–Zinc Deposits in the Southern Margin of the Altay*. Xinjiang. Geology Publishing House: Beijing; 1–210 (in Chinese).

Wang, J.B., **Zhang, J.H.**, **Ding, R.F.**, **Fang, T.H. 2000**. Tectono-metallogenic system in the Altay Orogenic Belt, China. *Acta Geologica Sinica* **74**, 485–491.

Wang, T., **Hong, D.W.**, **Tong, Y.**, **Han, B.F.**, **Shi, Y.R. 2005**. Zircon U–Pb SHRIMP age and origin of post-orogenic Lamazhao granitic pluton from Altay orogen: its implications for vertical continental growth. *Acta Petrologica Sinica* **21**, 640–650 (in Chinese with English abstract).

Wang, T., **Hong, D.W.**, **Jahn, B.M.**, **Tong, Y.**, **Wang, Y.B.**, **Han, B.F.**, **Wang, X.X. 2006**. Timing, petrogenesis, and setting of Palaeozoic synorogenic intrusions from the Altay Mountains, Northwest China:

implications for the tectonic evolution of an accretionary orogen. *The Journal of Geology* **114**, 735–751.

Wang, T., Tong, Y., Jahn, B.M., Zou, T.R., Wang, Y.B., Hong, D.W., Han, B.F. 2007. SHRIMP U–Pb Zircon geochronology of the Altay No. 3 Pegmatite, NW China, and its implications for the origin and tectonic setting of the pegmatite. *Ore Geology Reviews* **32**, 325–336.

Wang, T., Jahn, B.M., Kovach, V.P., Tong, Y., Hong, D.W., Han, B.F. 2009. Nd–Sr isotopic mapping of the Chinese Altay and implications for continental growth in the Central Asian Orogenic Belt. *Lithos* **110**, 359–372.

Wang, Y., Chen, Y.J., Ma, H.W., Xu, Y.L. 2009. Study on ore geology and fluid inclusions of the Tangjiaping Mo deposit Shangcheng County, Henan Province. *Acta Petrologica Sinica* **25**, 468–480 (in Chinese with English abstract).

Watters, W. 1958. Some zoned skarns from granite-marble contacts near Puyvalador, in the Quérigut area, eastern Pyrenees, and their petrogenesis. *Mineralogical Magazine* **31**, 703–725.

Windley, B.F., Alexeiev, D., Xiao, W., Kroner, A., Badarch, G. 2007. Tectonic models for accretion of the Central Asian Orogenic Belt. *Journal of the Geological Society* **164**, 31–47.

Xiao, W.J., Windley, B.F., Huang, B.C., Han, C.M., Yuan, C., Chen, H. L., Sun, M., Sun, S., Li, J.L. 2009. End-Permian to Mid-Triassic termination of the accretionary processes of the southern Altaids: implications for the geodynamic evolution, Phanerozoic continental growth, and metallogeny of Central Asia. *International Journal of Earth Sciences* **98**, 1189–1217.

Xu, L.G., Mao, J.W., Yang, F.Q., Li, J.G., Cai, Y.B., Zheng, J.M., Huang, C.L. 2007. Geology and geochemistry of the Mengku iron deposit in Fuyun County, Xinjiang Uigur Autonomous. *Acta Petrologica Sinica* **23**, 2653–2664 (in Chinese with English abstract).

Yang, Y.F., Li, N., Ni, Z.Y. 2009. Fluid inclusion study of the Jinduicheng porphyry Mo deposit, Hua county, Shanxi province. *Acta Petrologica Sinica* **25**, 2983–2993 (in Chinese with English abstract).

Yang, Y.F., Li, N., Chen, Y.J. 2012. Fluid inclusion study of the Nannihu giant porphyry Mo–W deposit, Henan Province, China: implications for the nature of porphyry ore-fluid systems formed in a continental collision setting. *Ore Geology Reviews* **46**, 83–94.

Yang, Y.F., Chen, Y.J., Zhang, J., Zhang, C. 2013a. Ore geology, fluid inclusions and four-stage hydrothermal mineralization of the Shangfanggou giant Mo–Fe deposit in Eastern Qinling, central China. *Ore Geology Reviews* **55**, 146–161.

Yang, Y.F., Chen, Y.J., Li, N., Mi, M., Xu, Y.L., Li, F.L., Wan, S.Q. 2013b. Fluid inclusion and isotope geochemistry of the Qian'echong giant porphyry Mo deposit, Dabie Shan, China: A case of NaCl-poor, CO_2-rich fluid systems. *Journal of Geochemical Exploration* **124**, 1–13.

Ye, Q.T., Fu, X.J. 1998. Metallogeny of polymetallic metallogenic belts on the southern margin of the Altay Mountains, Xinjiang, China. *Acta Geologica Sinica* **19**, 349–357 (in Chinese with English abstract).

Yuan, J.J., Wang, H.N., Zhang, H.J., Yang, X.F., Kang, J.C. 2011. Geological characteristics and prospecting range of Talate Fe–Pb–Zn deposit in Altay, Xinjiang. *Science and Technology Information* **23**, 61–65.

Zhang, L., Zheng, Y., Chen, Y.J. 2012. Ore geology and fluid inclusion geochemistry of the Tiemurte Pb–Zn–Cu deposit, Altay, Xinjiang, China: A case study of orogenic-type Pb–Zn systems. *Journal of Asian Earth Sciences* **49**, 69–79.

Zhang, L., Chen, H.Y., Zheng, Y., Qin, Y.J., Li, D.F. 2014. Geology, fluid inclusion and age constraints on genesis of the Sarekuobu gold deposit in Altay, NW China. *Geological Journal* **49**(6), 635–648. DOI: 10.1002/gj.2573

Zheng, C.Q., Kato, T., Enami, M., Xu, X.C. 2007. CHIME monazite ages of metasediments from the Altay orogen in northwestern China: Devonian and Permian ages of metamorphism and their significance. *Island Arc* **16**, 598–604.

Zheng, Y., Zhang, L., Chen, Y.J., Qin, Y.J., Liu, C.F. 2012. Geology, fluid inclusion geochemistry, and $^{40}Ar/^{39}Ar$ geochronology of the Wulasigou Cu deposit, and their implications for ore genesis, Altay, Xinjiang, China. *Ore Geology Reviews* **49**, 128–140.

Zheng, Y., Zhang, L., Guo, Z.L. 2013. Zircon LA–ICP–MS U–Pb and biotite $^{40}Ar/^{39}Ar$ geochronology of the Tiemuert Pb–Zn–Cu deposit, Xinjiang: implications for ore genesis. *Acta Petrologica Sinica* **29**, 191–204 (in Chinese with English abstract).

Zhou, M.F., Lesher, C.M., Yang, Z.X., Li, J.W., Sun, M. 2004. Geochemistry and petrogenesis of 270 Ma Ni–Cu–(PGE) sulphide-bearing mafic intrusions in the Huangshan district, Eastern Xinjiang, Northwest China: implications for the tectonic evolution of the Central Asian orogenic belt. *Chemical Geology* **209**, 233–257.